Marine Chemistry 221 (2020) 103773

Contents lists available at ScienceDirect

Marine Chemistry

journal homepage: www.elsevier.com/locate/marchem

Trace metal and nutrient dynamics across broad biogeochemical gradients in the Indian and Pacific sectors of the Southern Ocean

David J. Janssen[a,*], Matthias Sieber[b,c], Michael J. Ellwood[d], Tim M. Conway[c,e], Pamela M. Barrett[d], Xiaoyu Chen[d], Gregory F. de Souza[b], Christel S. Hassler[f], Samuel L. Jaccard[a]

[a] Institute of Geological Sciences & Oeschger Center for Climate Change Research, University of Bern, Switzerland
[b] Institute of Geochemistry and Petrology, ETHe Zürich, Zürich, Switzerland
[c] College of Marine Science, University of South Florida, St Petersburg, FL, USA
[d] Research School of Earth Sciences, Australian National University, Australia
[e] School of Geosciences, University of South Florida, Tampa, FL, USA
[f] Department F.-A. Forel for Environmental and Aquatic Science, University of Geneva, Switzerland

ARTICLE INFO

Keywords:
Trace Metal
Southern Ocean
GEOTRACES
Iron
Antarctic Circumnavigation Expedition

ABSTRACT

The Southern Ocean is the largest high-nutrient low-chlorophyll environment in the global ocean, and represents an important source of intermediate and deep waters to lower latitudes. Constraining Southern Ocean trace metal biogeochemical cycling is therefore important not just for understanding biological productivity and carbon cycling regionally, but also for understanding trace metal distributions throughout the lower latitude oceans. We present dissolved Fe, Ni, Cu, Zn, Cd, Pb and macronutrient concentrations in the Indian and Pacific sectors of the Southern Ocean from the Antarctic Circumnavigation Expedition (austral summer 2016-17), which included the first opportunities to study trace metal cycling at the Mertz Glacier Polynya and the Balleny Islands, as well as two meridional cross-frontal transects. Dissolved Ni, Cu, Zn, Cd and macronutrient concentrations show similar or greater variability latitudinally within surface waters than vertically through the water column, reflecting the combined influence of circulation and biological drawdown in shaping the distributions of nutrient-type elements in the Southern Ocean. Slopes of Cu-Si(OH)$_4$ and Cd-PO$_4$ increase from the Polar Frontal Zone to south of the Southern ACC Boundary (Cu-Si(OH)$_4$) and from the Subantarctic Zone to the Antarctic Zone (Cd-PO$_4$). Latitudinal differences are also observed for Ni-Si(OH)$_4$ and Zn-PO$_4$, with distinct Subantarctic Zone trends relative to those south of the Polar Front. Similarities between our Zn-Si(OH)$_4$ and Cd-PO$_4$ correlations and global compilations reflect the importance of exported Southern Ocean waters in setting these metal-macronutrient couples globally. Distinct Ni-macronutrient correlations are observed in this dataset relative to the global ocean, which supports a distinct cycling of Ni in the Southern Ocean compared to other basins. Concentrations of Pb are among the lowest observed in the global ocean; however, a local maximum is seen along the density level corresponding with Antarctic Intermediate Water. Concentrations within this isopycnal decrease with increasing latitude, which can be explained by decreasing atmospheric Pb input to more recently subducted waters.

Substantial biological uptake of metals and macronutrients is observed at the Mertz Glacier Polynya. Here, inferred metal:macronutrient uptake ratios are comparable to those found in the Amundsen Sea Polynya, in Southern Ocean phytoplankton, and to metal-macronutrient correlations in our data set as a whole, highlighting the potential of Southern Ocean polynyas as natural systems for trace metal uptake and export studies. The Balleny Islands are a source of Fe to surface waters and the islands also appear to influence distributions of Zn, Cu and macronutrients, which may reflect the combined impact of Fe supply on biological uptake, mixing, and scavenging in deeper waters. The Kerguelen Plateau is also a source of Fe, as previously identified. Throughout our dataset, the ferricline is found deeper than the nitricline, in agreement with existing data and indicating that Fe is less easily entrained into the surface ocean than NO_3. Additionally, Fe:NO_3 ratios in most samples throughout the water column are Fe-limiting (<0.01 mmol mol^{-1}). Therefore deep mixing, identified previously as the main Fe source to much of the Southern Ocean, would ultimately act to maintain Fe limitation.

* Corresponding author.
E-mail address: david.janssen@geo.unibe.ch (D.J. Janssen).

https://doi.org/10.1016/j.marchem.2020.103773
Received 16 August 2019; Received in revised form 3 February 2020; Accepted 23 February 2020
Available online 26 February 2020

1. Introduction

Surface waters of the Southern Ocean are characterized by high macronutrient concentrations (Garcia et al., 2014), partly due to the upwelling of nutrient-rich waters around Antarctica and partly to Fe, Si and light (co-)limitation leading to incomplete utilisation of nutrients in surface waters, denoted as a high-nutrient, low-chlorophyll (HNLC) state (e.g. Martin et al., 1990a; Coale et al., 2004; Boyd et al., 2007 and references therein; Hoffmann et al., 2008). The Southern Ocean is the largest Fe-limited, HNLC region in the world ocean (Moore et al., 2001, 2013; Mahowald et al., 2018). Changes in the supply of atmospheric Fe to this region over glacial-interglacial cycles, and even at millennial timescales, have been suggested to drive fundamental changes in the biological pump and carbon cycle in this region (Martin, 1990; Martínez-García et al., 2011; Jaccard et al., 2013), motivating much work focusing on the details of Fe cycling in the Southern Ocean. However, uncertainties remain regarding Fe inputs to the region and the relative role of upwelling supply versus episodic and localized Fe sources in driving biological export of carbon and, subsequently, the region's importance in the global carbon cycle (e.g. Boyd et al., 2007; Blain et al., 2007; Pollard et al., 2009; Lancelot et al., 2009; Lannuzel et al., 2011a; Tagliabue et al., 2014; Ardyna et al., 2019).

The Southern Ocean also plays an important role in driving biological productivity and biogeochemical cycling throughout the whole ocean system, with biological and physical surface processes in the Southern Ocean setting the characteristics of northward-moving water masses. The subduction of nutrient-rich Southern Ocean surface waters provides an important source of macronutrients to lower-latitude thermocline waters (e.g. Sarmiento et al., 2004). Additionally, differential biological uptake of trace metals and nutrients in different regions of the Southern Ocean, coupled with physical forcings, acts to partition elements between different northward-moving water masses, leaving intermediate waters with macronutrient:macronutrient, trace metal:macronutrient and isotope ratios that are distinct from deep waters (e.g. Sigman et al., 2000; Sarmiento et al., 2004; de Souza et al., 2012; Abouchami et al., 2014; Vance et al., 2017; Xie et al., 2017; Sieber et al., 2019a). Such processes have recently been shown to be pivotal in shaping the global Zn-Si relationship, as well as shaping the vertical profiles of dissolved Zn throughout the oceans (Vance et al., 2017; de Souza et al., 2018; Roshan et al., 2018; Weber et al., 2018). Similarly, the Southern Ocean plays an important role in driving the strong global correlation between Cd and PO_4 (Frew and Hunter, 1992; Frew, 1995; Baars et al., 2014; Quay et al., 2015; Middag et al., 2018; Sieber et al., 2019b), which has been explained by Fe-limitation in the Southern Ocean resulting in elevated uptake of Cd relative to PO_4 (Cullen et al., 2003; Quay et al., 2015). The importance of the Southern Ocean in driving nutrient and metal distributions, and the role of Fe in influencing both patterns of primary productivity and uptake of other trace metals and macronutrients in the Southern Ocean (Franck et al., 2000; Cullen et al., 2003; Twining et al., 2004; Boyd et al., 2007), highlight the need to better understand trace metal delivery, biogeochemical cycling, and export within the Southern Ocean.

Broadly speaking, the Southern Ocean can be subdivided into three zonal sectors based on connections to other major ocean basins – the Atlantic, Indian and Pacific sectors. Among these sectors, the Atlantic sector is the best characterized for trace metal distributions thanks to the efforts of the GEOTRACES program (Schlitzer et al., 2018) and other expeditions. Additional regional studies have investigated trace metal distributions and cycling in areas of the Indian sector of the Southern Ocean (e.g. seasonal ice zones near the Antarctic Continent: SIPEX and SIPEX-2; the Kerguelen Plateau: KEOPS and KEOPS-2; Crozet: CROZEX; Heard & Macdonald Islands: HEOBI) and in meridional transects from South Africa (GEOTRACES section GIPY05; CLIVAR section I06S), Australia (GEOTRACES section GIPY06) and the Indian Ocean (CLIVAR section I08S/I09N) to the Antarctic continent. Data from these and similar studies have helped to build an understanding of Southern Ocean trace metal distributions and the role of the Southern Ocean in global distributions of trace metals and their isotopes (e.g. Abouchami et al., 2014; Baars et al., 2014; Echegoyen et al., 2014; Roshan et al., 2018; Barrett et al., 2018) as well as an understanding of the impacts of regional features, especially localized lithogenic iron sources, on biological productivity and the biogeochemistry of other trace metals (e.g. Blain et al., 2001; Bakker et al., 2007; Lannuzel et al., 2011a; Grand et al., 2015; Sherrell et al., 2015; Ardyna et al., 2019; Holmes et al., 2019; Wang et al., 2019). However, the Pacific sector generally remains under-represented in trace metal data coverage of the Southern Ocean (Schlitzer et al., 2018).

Here, we present dissolved macronutrient (NO_3, PO_4, $Si(OH)_4$), Fe, Ni, Cu, Zn, Cd and Pb data covering the Indian and Pacific sectors of the Southern Ocean in the Austral summer of 2016–2017 from Legs 1 and 2 of the Antarctic Circumnavigation Expedition (ACE) (Walton and Thomas, 2018). This expedition, which sailed Cape Town – Hobart (Leg 1), Hobart – Punta Arenas (Leg 2) and Punta Arenas – Cape Town (Leg 3), provided the unique opportunity for near-contemporaneous characterization of multiple sectors of the Southern Ocean of trace metals at high depth resolution over the upper 1000 m, including meridional transects across frontal zones and the first trace metal sampling opportunities in two distinct Antarctic environments with potential continental influence: the Mertz Glacier Polynya and the Balleny Islands. Dissolved concentrations and stable isotope ratios from the ACE expedition have been published previously for Cr (Legs 1–2, Rickli et al., 2019), Zn (Legs 2–3, Sieber et al., 2020), and Cd (Legs 2–3, Sieber et al., 2019b).

2. Study area and oceanographic context

The Southern Ocean is characterized by the strong, eastward flowing Antarctic Circumpolar Current (ACC) and is separated from the lower latitude oceans by the strong gradients in temperature and salinity that define the subtropical front (STF) (e.g. Orsi et al., 1995). South of the STF, an additional series of fronts are found within the ACC (from N to S: the Subantarctic Front, SAF; the Polar Front, PF; and the Southern ACC Boundary, SACCB; Orsi et al., 1995). These divide the Southern Ocean into different zones: the Subantarctic Zone (SAZ, between the STF and SAF), the Polar Frontal Zone (PFZ, between the SAF and PF) and the Antarctic Zone (AZ, between the PF and SACCB). Representative positions of the STF, SAF, PF and SACCB from Orsi et al. (1995) are shown in Fig. 1, along with surface macronutrients from the World Ocean Atlas (Garcia et al., 2014).

These surface macronutrient concentrations highlight natural differences in nutrient regimes within the Southern Ocean, which come about as a consequence of its physical oceanography: wind-driven upwelling supplies nutrient-rich deep waters to the surface south of the PF in the ACC; once upwelled, these waters are transported laterally in the surface by Ekman transport, with nutrients being drawn down by biological uptake towards the north. The water upwelling within the ACC is predominantly Upper Circumpolar Deep Water (UCDW; e.g. Lumpkin and Speer, 2007; Talley, 2013), while Lower Circumpolar Deep Water is found just below the surface south of the SACCB (e.g. Orsi et al., 1995). In the northern reaches of the ACC, deep winter convection and subduction lead to the formation of the intermediate-depth, low-salinity water mass Antarctic Intermediate Water (AAIW), which exists as a salinity minimum at a water depth of ~1000 m north of the ACC (e.g. Hanawa and Talley, 2001).

Surface waters between the SAF and STF are characterized by a meridional gradient in NO_3 and PO_4 concentrations, with higher NO_3 and PO_4 concentrations found close to and south of the SAF and with concentrations decreasing to the north (see also, Fig. 1). In this region, biological productivity is limited by Fe (e.g. Boyd et al., 2007; Moore et al., 2013 and references therein). Low levels of $Si(OH)_4$ north of the SAF can also limit production by silicifying phytoplankton such as diatoms (Coale et al., 2004), and thus calcifiers such as

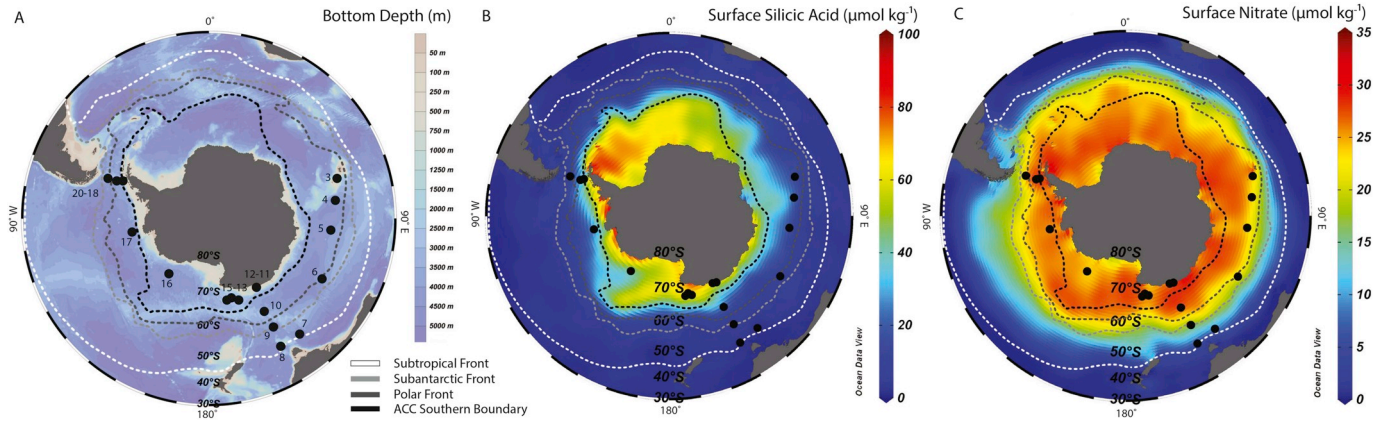

Fig. 1. (a) Sampling locations on Antarctic Circumnavigation Expedition Legs 1 and 2 in Austral Summer 2016–2017, and (b) & (c) surface macronutrients in the Southern Ocean. Representative positions of the STF, SAF, PF and SACCB (Orsi et al., 1995) are shown in white, light grey, dark grey and black dashed lines respectively. Station locations are shown as black circles and are numbered (a). Surface $Si(OH)_4$ (b) and NO_3 (c) are taken from the World Ocean Atlas, 2013 (Garcia et al., 2014).

coccolithophores typically play a larger role in surface phytoplankton community structure and in the export of organic matter to depth (Trull et al., 2001; Gibberd et al., 2013; Borges Mendes et al., 2015; Barrett et al., 2018). Surface NO_3 and PO_4 concentrations remain elevated while $Si(OH)_4$ concentrations remain low between the SAF and PF; however, diatom contributions to the surface community and to organic matter export increase near the SAF and in the PFZ (Trull et al., 2001; Kopczynska et al., 2001; Gibberd et al., 2013; Borges Mendes et al., 2015; Barrett et al., 2018). High macronutrient (NO_3, PO_4, $Si(OH)_4$) concentrations are found near to and south of the SACCB (Garcia et al., 2014), with Fe again acting to limit biological productivity (e.g. Martin et al., 1990a; Boyd et al., 2007). Within and south of the SACCB the phytoplankton community is dominated by diatoms, or by *Phaeocystis* near the ice edge (Gibberd et al., 2013; Borges Mendes et al., 2015).

In addition to these basin-wide gradients, mesoscale features including eddies (Jones et al., 2017), terrestrial input (e.g. Martin et al., 1990a; Ardelan et al., 2010; Gerringa et al., 2012) and polynya systems (e.g. Arrigo and van Dijken, 2003; Sambrotto et al., 2003) near the Antarctic continent, as well as Fe input and vertical mixing downstream of islands such as Kerguelen and Crozet (Blain et al., 2001; Bakker et al., 2007, respectively) are known to alter nutrient limitation dynamics and induce phytoplankton blooms. While localized Southern Ocean features impact the biological community and the biogeochemical cycles of certain elements, recent data identify that the distributions of some biologically-cycled elements may not show clear alteration due to such features (e.g. Zn, Ni; Wang et al., 2019). As part of ACE, we were able to sample downstream of both the Kerguelen Plateau and the Balleny Islands, as well as within the Mertz Glacier Polynya.

3. Methods

3.1. Sampling

Seawater samples were collected from the first two legs of the Antarctic Circumnavigation Expedition – Cape Town to Hobart (Leg 1, 20-December-2016 to 19-January-2017, stations 3–7) and Hobart to Punta Arenas (Leg 2, 22-January-2017 to 22-February-2017, stations 8–20) – onboard the R/V Akademik Tryoshnikov, organized by the Swiss Polar Institute.

Samples for trace metal measurements were collected using an autonomous rosette (Model 1018, General Oceanics, USA) on a Dyneema line equipped with acid-cleaned Teflon-coated 10 L Niskin bottles with external springs. Sampling from Niskin bottles was carried out onboard in a clean container with HEPA-filtered air. Samples were gravity-filtered through 0.2 μm acid-cleaned capsule filters (Acropak 200, Pall). We report concentrations from two different analytical methods and sample sets: 1) 250 mL samples collected for trace metal analysis and analyzed at Australian National University (ANU), and 2) 1–4 L samples collected for metal stable isotope analysis, processed at ETH Zurich (ETHZ) and analyzed at either ETHZ or the University of South Florida (USF).

Filtered samples for macronutrient analyses were also collected from trace metal rosette casts into 15 mL tubes and stored frozen until analysis ashore. CTD data (Fig. 2) are from a conventional CTD-rosette and are presented in Henry et al. (2019). Neutral density (γ^n) was calculated using Ocean Data View (Schlitzer, 2018).

3.2. Macronutrient analyses

Dissolved NO_x (NO_3 + NO_2), PO_4 and $Si(OH)_4$ were determined by flow-injection analysis (QuAAtro Seal Analytical auto-analyzer following Seal analytical methods) at the Alfred Wegener Institute (Germany). Calibration was performed using Certipur solutions (standard reference materials from the National Institute of Standards and Technology) and limits of detection were 0.16, 0.013, 0.07 μmol L^{-1} for NO_x, PO_4 and $Si(OH)_4$, respectively. Analytical accuracy was verified using certified reference materials (KANSO LTD, Japan) and measurements were within at least 90% of the certified values (not shown). Dissolved NO_2 was minimal (maximum 2.1% of NO_x, typically $<1\%$, not shown), and therefore NO_x is presented here as NO_3. Macronutrient data for the ACE voyage are available from Hassler and Ellwood (2019), and have been previously published in Rickli et al. (2019), Sieber et al. (2019b) and Sieber et al. (2020).

3.3. ANU samples, processing and analysis

Samples for trace metal concentrations were collected into 250 mL LDPE bottles acidified with HNO_3 to pH <1.8 and stored for at least 6 months before analysis. All ANU sampling bottles were acid-cleaned prior to use with 10% w/w aqua regia for one week followed by a second week in 1% w/w HNO_3. Bottles were stored full with 0.1% w/w HNO_3 until use. All onshore work was carried out under trace-metal clean conditions in ISO 5 clean hoods, using ultrapure reagents. Dissolved trace metal concentrations for Leg 1 (Fe, Ni, Cu, Zn, Cd) and Leg 2 (Ni, Cu, Cd, Pb) were determined at ANU by isotope dilution. Samples were pre-concentrated and the seawater matrix was removed offline using a home-built, automated pre-concentration system (Ellwood et al., 2018). Weighed sample aliquots were spiked with enriched isotopes (^{57}Fe, ^{61}Ni, ^{65}Cu, ^{67}Zn, ^{110}Cd, ^{206}Pb) and internal standards (Sc, In, Yb). Equilibrated samples were buffered to pH ≈ 5

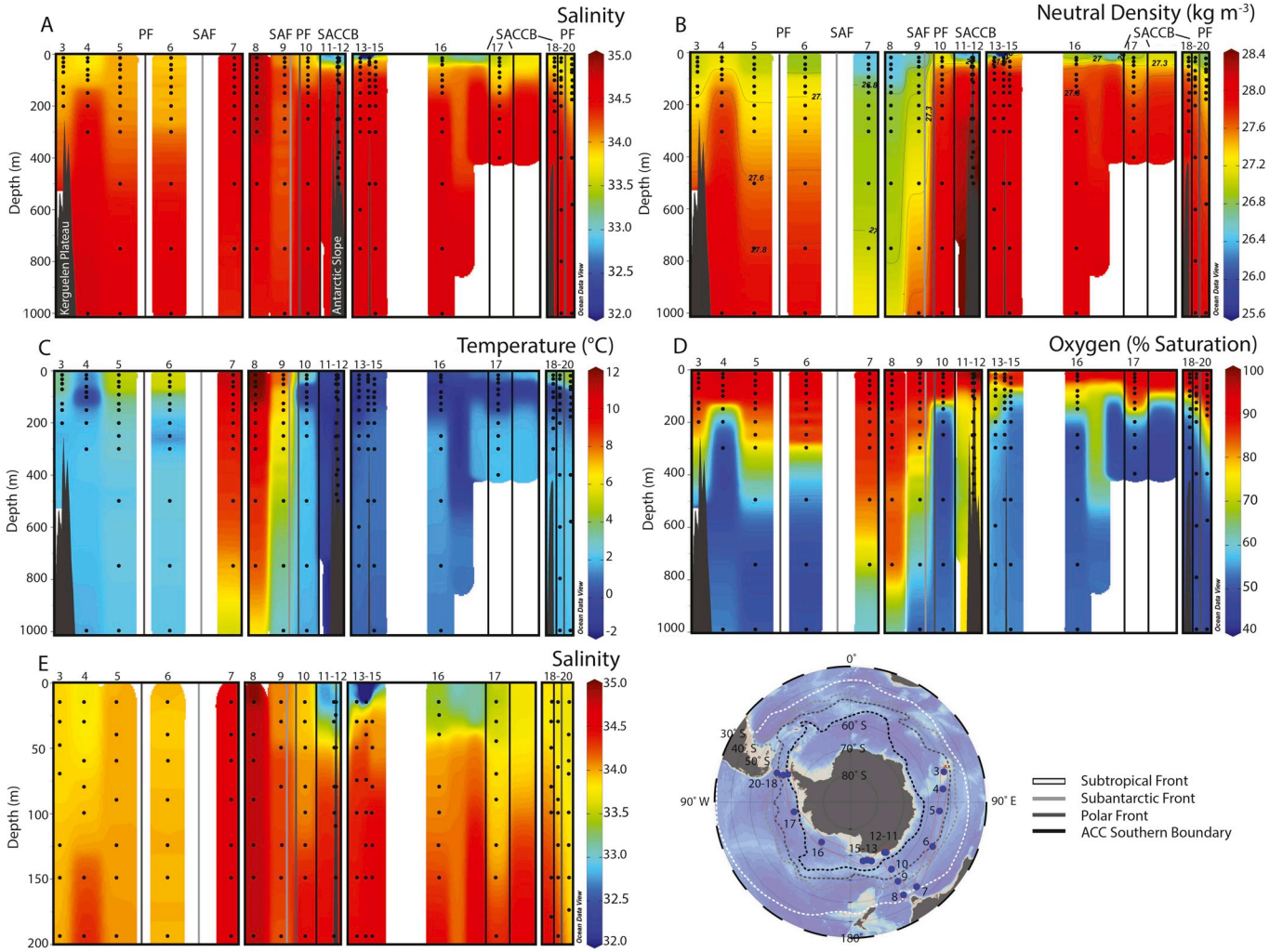

Fig. 2. ACE Legs 1 and 2 CTD data. Salinity (a), neutral density (γ^n) (b), temperature (c), and % oxygen saturation (d) are shown to 1000 m. Panel (e) shows salinity to 200 m depth. Positions of fronts (SAF, PF and SACCB; labelled) are shown as solid lines with colors matching the fronts in Fig. 1. Plots are broken by white bars to differentiate primarily zonal sections (stations 3–7, 12–18) and primarily meridional sections (stations 8–12, 18–20). Trace metal sample depths are shown as black circles. A map, with the ACE TM stations (blue circles, numbered) and the section for which CTD data are shown (red box) is at the bottom right, with dashed lines indicating front positions as in Fig. 1. The Kerguelen Plateau and the Antarctic Slope are labeled in plot (a). Salinity, temperature and oxygen data are from a conventional CTD-rosette, and neutral density was calculated using Ocean Data View (Schlitzer, 2018). (For interpretation of the references to colour in this figure legend, the reader is referred to the web version of this article.)

using an ammonium acetate buffer or to pH ≈ 7 with MOPS buffer (3-(N-morpholino)propansulfonic acid) and loaded onto a column filled with Nobias Chelate PA1 resin (Sohrin et al., 2008). After removal of the seawater matrix, samples were eluted in 1 M HNO_3 and analyzed by inductively coupled mass spectrometry (ICP-MS) on either a *Neptune* or *Element XR* instrument (both ThermoScientific).

3.4. ETHZ and USF samples, processing and analysis

Seawater samples (1–4 L) collected for Fe, Zn and Cd concentrations and isotopic composition, from which data for dissolved Fe and Zn concentration from Leg 2 are reported here, were acidified with 12 M Teflon-double-distilled HCl to pH ≈ 2, and stored for at least 3 months prior to processing. LDPE bottles for metal isotope samples were cleaned using standard trace metal cleaning methods following Conway et al. (2013).

Seawater dissolved Fe and Zn concentrations for Leg 2 were measured on samples taken for metal stable isotope composition and were processed at ETH Zurich in a Class 100 clean environment: acidified 1–4 L samples were amended with Fe and Zn double spikes, metal extracted by Nobias PA1 resin and metals purified using AG-MP1 resin, following previously published methods (Conway et al., 2013; Sieber et al., 2019a). Zn concentrations and isotope ratios were analyzed at ETHZ using a *Neptune Plus* MC-ICP-MS instrument (ThermoScientific), using an Aridus II desolvating system, and H-type sampler and skimmer Ni cones, following Archer et al. (2017). Fe concentrations and isotope ratios were analyzed at the University of South Florida using a Neptune Plus, with Apex-Omega desolvating system, a Jet Ni sampler cone and an X-type Al skimmer cone. Concentrations and isotope ratios for Zn and Cd from these samples are reported elsewhere (Sieber et al., 2019b; Sieber et al., 2020).

3.5. Accuracy and analytical metrics

Analyses of Cu, Ni, Cd and Pb in standard reference materials for the ANU concentration method (Legs 1 and 2) are shown in Table 1. Accuracy of Fe and Zn from the ANU concentration method (Leg 1) are demonstrated by the good agreement with previously published concentration data from the Southern Ocean Time Series (SOTS) site, which was sampled as station 7 during the ACE expedition (Supplemental Fig. 1, Ellwood et al., 2020). For Leg 2 Fe and Zn data (ETHZ/USF method), dissolved Fe (Table 1) and Zn (Table 1, from Sieber et al.,

Table 1
Analyses of GEOTRACES standard reference materials. Measured SAFe values for the ANU and ETHZ/USF methods are compared to consensus values (from www.geotraces.org). Data from GT09–17 bottle #2671 (3500 m depth, 2008 GEOTRACES IC1 cruise at BATS) compare well with previously published values (e.g. Cu, Cd, Pb - Lee et al., 2011; Cd, Pb - Boyle et al., 2012; Pb - Anderson et al., 2014). On the analytical day for the third SAFe D1 407 sample as well as the SAFe S and SAFe D2 samples, problems were encountered for Cd. No Cd data are used from this day. However, the other SAFe D1 #407 values, the GT09–17 values and the intercomparison shown in Supplemental Fig. 2 (with data from Sieber et al., 2019b) confirm that Cd values from other analytical days are accurate. Because SAFe standard data are not available, a comparison of Leg 1 Fe and Zn data (ANU method) with literature data at a crossover station is shown in Supplemental Fig. 1 for intercalibration purposes.

ANU (Legs 1 & 2: Cu, Ni, Cd, Pb)					**ETHZ/USF (Leg 2: Fe & Zn)**		
	Cu	Ni	Cd	Pb		Fe	Zn
	nmol kg^{-1}	nmol kg^{-1}	pmol kg^{-1}	pmol kg^{-1}		nmol kg^{-1}	nmol kg^{-1}
SAFe D1	2.10	8.77	1008	24.1	SAFe D1	NA	7.724
	2.14	8.76	1031	25.3			
	2.29	8.99	NA	24.3			7.461
Average	**2.17 ± 0.10**	**8.84 ± 0.13**	**1043 ± 42**	**24.8 ± 0.8**	**Average**		**7.59 ± 0.19**
Consensus	**2.27 ± 0.11**	**8.58 ± 0.26**	**991 ± 31**	**27.7 ± 2.6**	**Consensus**		**7.40 ± 0.35**
SAFe S	0.53	2.52	NA	42.2	SAFe D2	0.95	7.556
SAFe S Consensus	**0.52 ± 0.05**	**2.28 ± 0.09**	**1.1 ± 0.03**	**48 ± 2.2**			7.489
SAFe D2	2.78	8.99	NA	27.0	**Average**		**7.52 ± 0.05**
SAFe D2 Consensus	**2.28 ± 0.15**	**8.63 ± 0.25**	**986 ± 23**	**27.7 ± 1.5**	**Consensus**	**0.933 ± 0.023**	**7.43 ± 0.25**
GT09–17	1.87	4.52	311	16.6	NA	NA	NA
	1.83	4.59	300	18.1			

2020) concentrations measured on SAFe samples prepared during the same time as the ACE samples agree with consensus values. Uncertainty is estimated to be ~2% for the ETHZ/USF method (Conway et al., 2013). Additionally, Cd concentration data presented here for Leg 2 (ANU method) compare excellently with Cd concentrations measured on the Cd stable isotope samples for Leg 2 (ETHZ/USF method) and reported elsewhere (Sieber et al., 2019b; Supplemental Fig. 2).

4. Results & discussion

4.1. Macronutrients

Consistent with previous studies, distributions of dissolved PO_4, NO_3 and $Si(OH)_4$ in our dataset are typical of Fe-limited HNLC conditions throughout the Southern Ocean and consistent with the differing biogeochemical regimes in different Southern Ocean zones (e.g. Sarmiento et al., 2004; Coale et al., 2004; Garcia et al., 2014). Surface dissolved NO_3 and PO_4 concentrations increase in the SAZ approaching the SAF (from <10 to ~19 μmol kg^{-1} and <0.8 to ~1.2 μmol kg^{-1}, respectively), and continue to increase to the south of the PF, where surface concentrations stabilize at around 25 μmol kg^{-1} and 1.7 μmol kg^{-1}, respectively. In contrast, surface $Si(OH)_4$ concentrations are elevated in surface waters only south of the SACCB (Fig. 3). With the exception of stations 11 and 12, which are in the Mertz Glacier Polynya, all stations south of the SACCB show minimal NO_3 and PO_4 differences within depth profiles (surface:subsurface concentrations ≥0.8), suggesting limited surface biological drawdown at the time of sampling.

The most northerly stations, stations 7 and 8 in the SAZ, show low macronutrient concentrations at depth compared to other stations. South of the PF at ≥400 m, NO_3 and PO_4 concentrations are similar across all stations (NO_3 ~30–33 μmol kg^{-1}; PO_4 ~1.8–2.2 μmol kg^{-1}), though concentrations are slightly higher downstream of the Kerguelen Plateau and in the Drake Passage (up to NO_3 ~35 μmol kg^{-1} and PO_4 ~2.4 μmol kg^{-1}) (Fig. 3). This may reflect the impact of subsurface waters from the Pacific and Indian Oceans and greater total respiration of biogenic material as these stations correspond with lower O_2 (Fig. 2, see also apparent oxygen utilization in Supplemental Fig. 3). Dissolved Si $(OH)_4$ is highest in deep waters near the Balleny Islands (stations 13 and 15, up to 120 μmol kg^{-1}) (Fig. 3, Supplemental Fig. 7). These samples are enriched in $Si(OH)_4$ relative to other samples from similar isopycnals in the Pacific sector south of the SACCB, and may reflect a local circulation feature. A similar local $Si(OH)_4$ maximum is seen downstream of the Kerguelen Plateau at station 4, and has been reported previously (Fripiat et al., 2011). The Mertz Glacier Polynya shows relative $Si(OH)_4$ enrichment at stations 11 and 12 compared to the $Si(OH)_4$-NO_3 relationship observed elsewhere on the transect (Fig. 4), which may be due to Fe supply altering biological uptake ratios (e.g. Hutchins and Bruland, 1988) and/or to a local Si source (see Section 5.1). Si*, defined as the difference between observed $Si(OH)_4$ and NO_3 concentrations, generally follows $Si(OH)_4$ concentration trends. Si* ≤ −10 μmol kg^{-1} is indicative of SAMW (Sarmiento et al., 2004) and reflects the presence of this water mass in surface waters of Station 6 as well as below 100 m at stations 7 and 8. Si* is >20 μmol kg^{-1} below 400 m for all stations except 7 and 8, with maxima found in deeper samples on the Kerguelen Plateau, south of the SACCB near the Balleny Islands (Stations 14 and 15), and at station 16 (Fig. 3).

4.2. Iron

Dissolved Fe concentrations were below ~0.2 nmol kg^{-1} in the upper 100 m at most stations (Fig. 3), and reach as low as <0.05 nmol kg^{-1}, suggestive of Fe-limitation and in agreement with previously reported dissolved Fe distributions in the open Southern Ocean (e.g. de Baar et al., 1999; Measures and Vink, 2001; Ellwood et al., 2008; Sedwick et al., 2008; Bowie et al., 2009; Klunder et al., 2011; Grand et al., 2015). The Fe:NO_3 ratio, which remains ≤0.01 mmol mol^{-1} at most stations away from local Fe sources, also suggests Fe-limiting conditions. The Fe:NO_3 trends are discussed in detail in Section 5.4. Dissolved Fe concentrations above 0.25 nmol kg^{-1} are found at all stations at ≥400 m, except for stations 7 and 8 in the SAZ, where Fe concentrations generally remained around or below 0.2 nmol kg^{-1} to the bottom of the sampled profile at 1000 m. Dissolved Fe depth profiles are punctuated by local subsurface Fe sources on the Kerguelen Plateau, Balleny Islands, the Mertz Glacier Polynya and near the Antarctic Peninsula south of the Drake Passage.

Higher surface or near-surface (~100–300 m) Fe concentrations (0.4–0.7 nmol kg^{-1}) are found at stations on the Kerguelen Plateau (Stations 3 and 4) and near the Balleny Islands (Stations 13–15), with enrichments up to 0.8 nmol kg^{-1} also apparent in deeper samples at these stations (Fig. 3). Elevated Fe near these islands is indicative of local Fe sources, as has been well documented previously at the

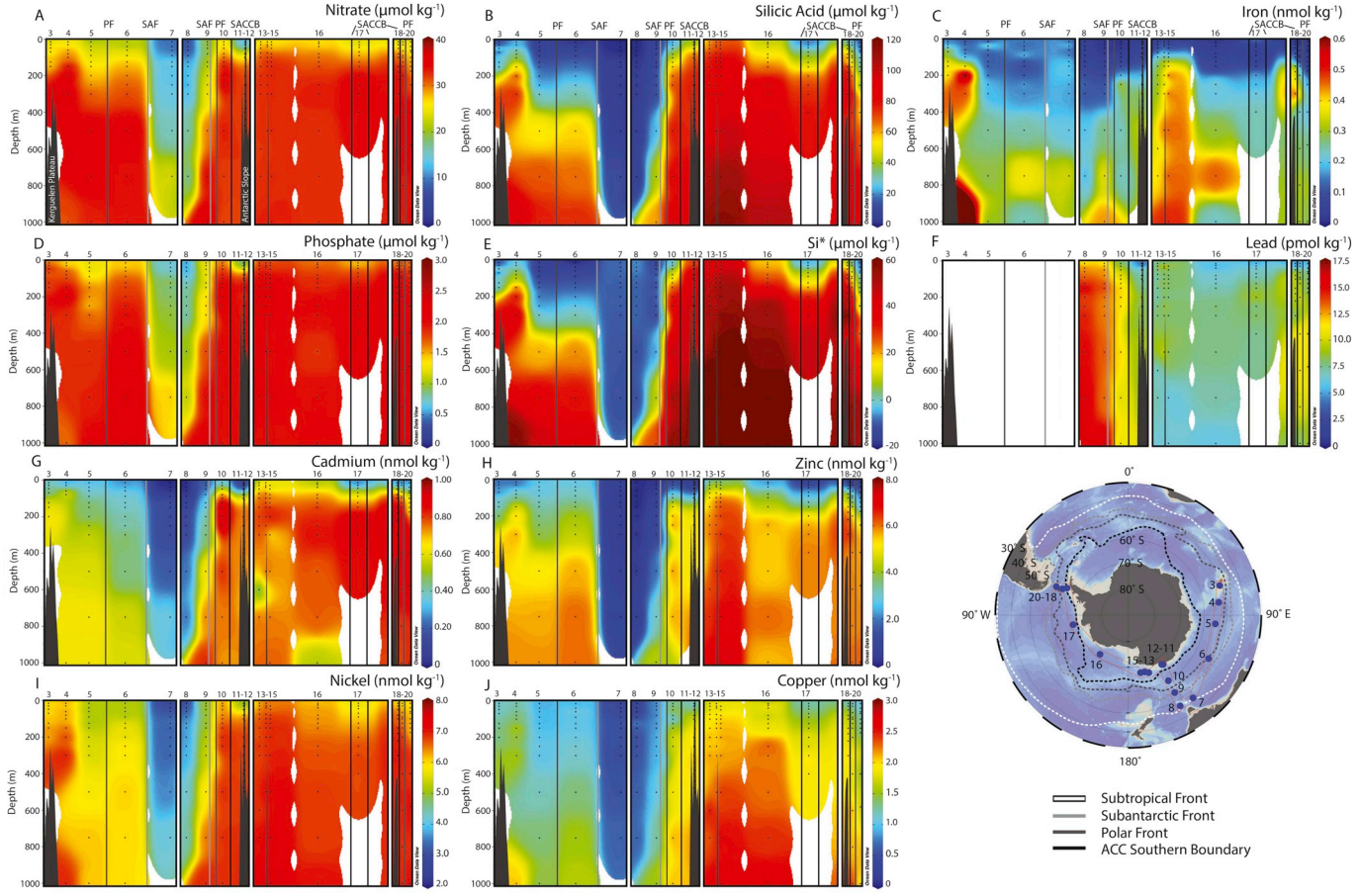

Fig. 3. ACE Leg 1 and 2 dissolved trace metal and macronutrient concentrations. Section plots are shown for trace metal and macronutrient concentrations to 1000 m along the cruise track. Sample locations are denoted in the section plots as black circles, and stations are numbered above the plots. Section plots are as follows: NO_3 (a), $Si(OH)_4$ (b), Fe (c), PO_4 (d), Si* (e) ($Si(OH)_4 - NO_3$, Sarmiento et al. (2004)), Pb (f), Cd (g), Zn (h), Ni (i), Cu (j). Positions of fronts (SAF, PF and SACCB; labelled) are shown as solid lines with colors matching the fronts in Fig. 1. Plots are broken by white bars to differentiate primarily zonal sections (stations 3–7, 12–18) and primarily meridional sections (stations 8–12, 18–20). The map at the bottom right shows the plotted section (red box) with stations as blue circles and numbered. Dashed lines indicate front positions as in Fig. 1. Lead data are not available for Leg 1 (stations 3–7). The Kerguelen Plateau and the Antarctic Slope are labeled in plot (a). (For interpretation of the references to colour in this figure legend, the reader is referred to the web version of this article.)

Kerguelen Plateau and other Southern Ocean islands (e.g. Blain et al., 2001; Bakker et al., 2007; Blain et al., 2008; Holmes et al., 2019). Elevated Fe concentrations (~0.5 nmol kg^{-1}) are also found below 100 m at station 18. This station is in shallower waters near the shelf break of the Antarctic Peninsula, and likely reflects local sedimentary input on the West Antarctic Peninsula, which has been documented previously (e.g. Ardelan et al., 2010; de Jong et al., 2012; Hatta et al., 2013). The importance of localized shelf and island Fe sources to the wider region remains poorly constrained, although studies suggest potential long-distance Fe transport (e.g. Bucciarelli et al., 2001; de Jong et al., 2012; Measures et al., 2013; Grand et al., 2015; Schallenberg et al., 2018). Finally, the Mertz Glacier Polynya shows enriched Fe from 200–500 m (up to 0.4 nmol kg^{-1}), though to a lesser degree than the stations discussed above. The influence of the Mertz Glacier Polynya, and of the Kerguelen & Balleny Islands, on all the nutrients and trace metals is discussed in more detail in sections 5.1 and 5.2, respectively.

4.3. Zinc and cadmium

Dissolved Zn and Cd distributions correlate strongly with the macronutrients $Si(OH)_4$ and PO_4, respectively (Figs. 3 & 4), as described in the first oceanic profiles of these metals, as well as in more recent GEOTRACES data (e.g. Boyle et al., 1976; Bruland et al., 1978; Bruland, 1980; Baars et al., 2014; Wyatt et al., 2014; Middag et al., 2018; Schlitzer et al., 2018; Middag et al., 2019). Strong latitudinal variability in dissolved Zn and Cd concentrations is observed in surface waters from the SAZ to the PF, as seen previously in the Southern Ocean (e.g. Löscher, 1999; Ellwood et al., 2008; Croot et al., 2011; Boye et al., 2012; Baars et al., 2014; Cloete et al., 2018), reaching a similar magnitude to the surface-to-1000 m concentration gradients. In the SAZ, the minimum dissolved Zn and Cd concentrations are <0.1 nmol kg^{-1} and <10 pmol kg^{-1}, respectively. Similar Zn concentrations have previously been found to be limiting or co-limiting in the open ocean (Chappell et al., 2016). Elevated surface Zn and Cd concentrations are found south of the PF, as observed previously (e.g. Croot et al., 2011; Boye et al., 2012; Baars et al., 2014; Cloete et al., 2018), extending up to maxima of ~2 nmol kg^{-1} and ~0.5 nmol kg^{-1}, respectively. This is roughly half of the global deepwater Cd maximum but only ~20% of the global deepwater Zn maximum (Figs. 3 & 4). This contrast between Zn and Cd mirrors the differing distributions of $Si(OH)_4$ versus PO_4 and NO_3 in the Southern Ocean (Sarmiento et al., 2007), and reflects the unique cycling of Zn and $Si(OH)_4$ in the Southern Ocean relative to other nutrient-type elements, perhaps due to the influence of high Zn uptake during Fe-limited diatom growth (see also Sarmiento et al., 2004; Vance et al., 2017; de Souza et al., 2018; Roshan et al., 2018). Stations 11 and 12, near Mertz Glacier, have lower surface dissolved Zn and Cd concentrations than other stations south of the PF (see Section 5.1).

Depth profiles in the SAZ show low Zn concentrations (<1 nmol kg^{-1}) in the upper 1000 m, in agreement with previous data

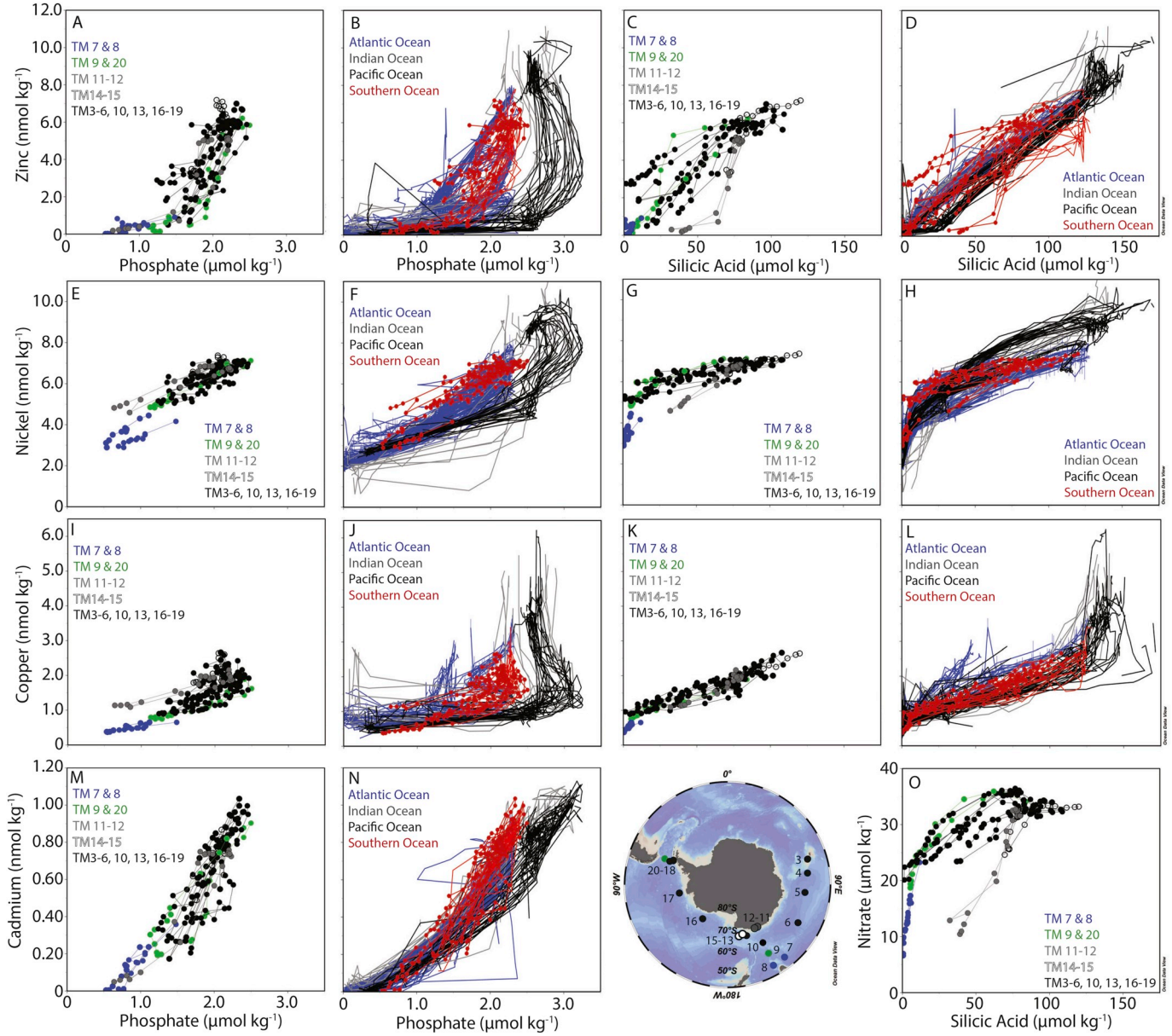

Fig. 4. Dissolved metal-macronutrient relationships in the ACE dataset. Relationships between trace metals and macronutrients (Me-PO_4 and Me-$Si(OH)_4$ for Zn, Cu and Ni; only Me-PO_4 for Cd) are shown for the ACE transect (first and third columns and panel o) and for the global ocean (second and fourth columns, except panel o), based on paired metal-macronutrient measurements from this study and the GEOTRACES Intermediate Data Product, 2017 (Schlitzer et al., 2018). For the ACE data, Stations 7 and 8 (in the SAZ) are shown in blue, station 9 and 20 (near the SAF) are shown in green, stations 11 and 12 (Mertz Glacier Polynya) are shown in grey, and stations 14 and 15 (near the Balleny Islands) are shown as open symbols. All other stations are in black. For the global compilation plots, the Southern Ocean data are shown in red, Atlantic Ocean in blue, Pacific Ocean in black and Indian Ocean in grey. Plotted elements and scaling are consistent between all x-axes for one column, and for all y-axes for one row except in panel (o), and therefore not every axis is labeled. Panel (o) shows $Si(OH)_4$-NO_3 from this study. A full reference list from the GEOTRACES Intermediate Data Product is shown in Supplemental Table 4. (For interpretation of the references to colour in this figure legend, the reader is referred to the web version of this article.)

from the Indian sector (Ellwood, 2008); however, Zn concentrations ~4 times higher have been reported in the Atlantic sector (Croot et al., 2011; Cloete et al., 2018). Depth profiles for dissolved Cd in the SAZ span a much larger range (up two orders of magnitude), as reported previously (e.g. Ellwood, 2008; Baars et al., 2014; Sieber et al., 2019a). The highest subsurface dissolved Cd concentrations are found near the γ^n = 27.8 kg m^{-3} isopycnal between the PF and the SACCB in the Pacific sector and the Drake Passage (Stations 10, 17, 19; Figs. 2 & 3), in good agreement with data from the Atlantic sector (Baars et al., 2014). Dissolved Cd maxima in the Pacific Sector between the PF and SACCB are higher than the maxima between these fronts in the Indian sector, even at similar γ^n and O_2. The reason for this difference remains unclear; however, we find the same trend for Cu and Zn, and therefore there may be a basin-scale, hydrographic control. We find slightly higher Zn on the shelf break to the south of the Drake Passage (station 18) and within it (stations 19–20) – up to 7 and ~6.3 nmol kg^{-1}, respectively – than reported previously in the upper 1000 m in this area (up to ~5.5 nmol kg^{-1}, Martin et al., 1990b; ~5 nmol kg^{-1}, Croot et al., 2011). This may be related to the station locations, e.g. proximity to the Antarctic Peninsula, or to methodological differences resulting in the underreporting of values (in Croot et al., 2011; as noted in Zhao et al., 2014). The highest subsurface Zn concentrations in our dataset are found near to, and downstream of, the Balleny Islands (Figs. 3 & 4), which may reflect a lithogenic source, changes to biological cycling, or

Table 2
Metal-macronutrient regressions. Metal-macronutrient regression slopes and intercepts, r^2 values and number of samples used in the regression (n) are presented for this study and for the global ocean. Regression slopes for this study are presented with 1 standard error. Global data are from paired metal and macronutrient measurements from this study and the GEOTRACES 2017 Intermediate Data Product (Schlitzer et al., 2018). Regression data under multiple station subsets are presented when Me-macronutrient distributions are not uniform across different zones (e.g. the SAZ, PFZ, AZ and south of the SACCB) or stations with deviations from the general trend were observed (e.g. surface samples at stations 11 and 12 – see Section 5.1, stations 7 and 8). Data are shown in Fig. 4. A full reference list from the GEOTRACES Intermediate Data Product is shown in Supplemental Table 4.

Me-Macronutrient	This study				Global Ocean			
	Slope	r^2	b	n	Slope	r^2	b	n
	nmol μmol^{-1}		nmol		nmol μmol^{-1}		nmol	
Zn-Si(OH)$_4$	0.060 ± 0.002	0.77	0.66	191	0.059	0.97	0.26	3963
Zn-Si(OH)$_4$, not stns 11–12	0.061 ± 0.002	0.83	0.78	170				
Zn-PO$_4$ (PO$_4$ ≤ 1.2 μmol kg^{-1})	0.31 ± 0.20	0.08	−0.05	29	0.95	0.67	0.00	1212
Zn-PO$_4$ (PO$_4$ ≥ 1.2 μmol kg^{-1})	5.08 ± 0.34	0.58	−5.52	162	3.17	0.61	−2.53	2493
Cd-PO$_4$	0.53 ± 0.02	0.84	−0.36	189	0.354	0.96	−0.113	3657
Cd-PO$_4$, stns 7 & 8	0.41 ± 0.04	0.85	−0.22	22				
Cd-PO$_4$, PFZ	0.57 ± 0.07	0.74	−0.59	23				
Cd-PO$_4$, AZ	0.65 ± 0.04	0.79	−0.56	58				
Cd-PO$_4$, South of SACCB*	0.57 ± 0.05	0.65	−0.41	68				
Ni-PO$_4$	2.13 ± 0.07	0.83	2.30	194	2.19	0.91	1.78	2945
Ni-PO$_4$, stns 7–8 only	1.21 ± 0.36	0.35	2.49	22				
Ni-Si(OH)$_4$, not stns 7–8	0.018 ± 0.001	0.71	5.33	172	0.044	0.92	3.28	3201
Ni-Si(OH)$_4$, not stns 7–8, 11–12	0.018 ± 0.001	0.77	5.40	150				
Ni-Si(OH)$_4$, stns 7–8	0.12 ± 0.03	0.47	3.12	22				
Cu-Si(OH)$_4$	0.016 ± 0.000	0.90	0.69	191	0.019	0.9	0.68	2506
Cu-Si(OH)$_4$, stns 7 & 8	0.028 ± 0.004	0.75	0.41	21				
Cu-Si(OH)$_4$, not stns 7 & 8	0.015 ± 0.000	0.89	0.80	170				
Cu-Si(OH)$_4$, PFZ	0.010 ± 0.001	0.93	0.90	23				
Cu-Si(OH)$_4$, AZ	0.012 ± 0.001	0.80	0.91	61				
Cu-Si(OH)$_4$, South of SACCB*	0.015 ± 0.001	0.76	0.83	68				

PFZ = station 6, 20.
AZ = Stations 3–5, 10, 17, 19.
South of the SACCB = Stations 11–16, 18.
* Does not include station 11 ≤ 25 m, station 11 ≤ 50 m.

local circulation (see also Section 5.2).

The Zn-Si(OH)$_4$ correlation in our data (0.060 ± 0.002 mmol mol^{-1}) corresponds very well with the global Zn-Si(OH)$_4$ relationship from paired Zn and Si(OH)$_4$ measurements in the GEOTRACES intermediate data product (0.059 mmol mol^{-1}, Schlitzer et al., 2018) (Table 2, Fig. 4c and d), with data from the Drake Passage (Martin et al., 1990b), and with some data from the Atlantic sector (Zhao et al., 2014; Cloete et al., 2018 wintertime data), but our observed slope is higher than reported in other datasets from the Atlantic sector of the Southern Ocean (0.033–0.048 mmol mol^{-1}, Löscher, 1999; Croot et al., 2011; Cloete et al., 2018 summer data). Stations 5 and 6, near to but south of the PF in the Indian sector, fall above the Zn-Si(OH)$_4$ trend found at the rest of the stations (Fig. 4(c)). This is only apparent in the upper 300 m (Si(OH)$_4$ < 40 μmol kg^{-1}), and was not observed at stations 3 and 4 or in previous data in the Indian sector (Wang et al., 2019). In contrast, Ni-Si(OH)$_4$ and Si(OH)$_4$-NO$_3$ trends for these samples do not diverge from the rest of the data (Fig. 4g and o), suggesting that this Zn-Si(OH)$_4$ divergence is caused by additional Zn. The reason for this is unclear. In contrast to these high-Zn samples, samples near Mertz Glacier (stations 11 and 12) fall below the Zn-Si(OH)$_4$ trend. This may reflect different metal and macronutrient cycling, including increased biological uptake of Zn relative to Si(OH)$_4$, or possible continental input of Si(OH)$_4$. The Si(OH)$_4$-NO$_3$ relationship at these stations is also distinct from that in the rest of our data (Fig. 4o), supporting either differences in biological uptake ratios here or local sources.

The Zn-PO$_4$ trend shows strong latitudinal differences, with low Zn-PO$_4$ slopes at low PO$_4$ concentrations (0.31 ± 0.20 mmol mol^{-1}, primarily based on waters in the SAZ) and elevated slopes at higher PO$_4$ concentrations (5.1 mmol mol^{-1}, primarily based on waters south of the PF) (Table 2, Fig. 4a and b). This has been described previously and relates to the elevated biological uptake of Zn relative to PO$_4$ and the coupled biogeochemical cycling of these elements in the Southern Ocean (Vance et al., 2017; de Souza et al., 2018; Roshan et al., 2018). The high-slope trend (5.08 ± 0.34 mmol mol^{-1}) is similar to that previously described in the Atlantic Ocean and attributed to advected Southern Ocean waters (4.6 mmol mol^{-1}, Wyatt et al., 2014) (Fig. 4a and b). A kink is observed in the Zn-PO$_4$ relationship at stations 11 and 12 in the Mertz Glacier Polynya, which may reflect changes in biological productivity and the degree of Fe limitation at these sites (see section 5.1) as well as the mixing between Zn-depleted surface waters with Zn and PO$_4$-rich subsurface waters.

Our Southern Ocean data demonstrate a strong linear Cd-PO$_4$ relationship with a much higher slope (0.53 ± 0.02 mmol mol^{-1}) than the global average trend (0.35 mmol mol^{-1}) (Table 2; Fig. 4m and n). Indeed, the Cd-PO$_4$ trends we observe are among the steepest found in any ocean basin (Fig. 4n), in agreement with previously reported high slopes for the Southern Ocean (e.g. Nolting et al., 1991; Frew and Hunter, 1992; de Baar et al., 1994; Frew, 1995; Baars et al., 2014; Quay et al., 2015). High Cd-PO$_4$ slopes are also consistent with biological Cd uptake, export and remineralization in chronically Fe-limited regions such as the Southern Ocean, where high Cd:PO$_4$ uptake ratios are observed (e.g. Cullen et al., 2003; Cullen, 2006; Quay et al., 2015). While there is a good correlation for the single Cd-PO$_4$ trend including all our data, latitudinal variability is also apparent. Stations 7 and 8, in the SAZ, have a lower slope (0.41 ± 0.04 mmol mol^{-1}) than zones to the south and than the composite trend (Table 2). Differences in regression slopes between the PFZ, AZ and south of the SACCB are not observed considering regression uncertainty; however, distinct regression slopes have been reported in water masses originating in the Southern Ocean (Baars et al., 2014; Middag et al., 2018; Sieber et al., 2019b) and more robust zonal differences observed within the Southern Ocean may be apparent as more data become available. Stations near the Mertz Glacier Polynya demonstrate a slight kink near PO$_4$ = 1.5 μmol kg^{-1}

(Fig. 4), which likely reflects changes in biological uptake and/or differences between nutrient-depleted surface waters and subsurface waters, as for Zn-PO_4 trends. Cadmium and Zn data are discussed further, including with stable isotope composition, in Sieber et al. (2019b, 2020), respectively.

4.4. Copper and nickel

Both dissolved Cu and Ni show typical nutrient-type depth profiles as seen in other basins, with surface depletion and enrichments at depth; however, the dynamic range (i.e. surface-to-deep concentration gradients) is more limited compared to macronutrients and other nutrient-type metals like Zn and Cd, as in other parts of the global ocean (e.g. Sclater et al., 1976; Bruland, 1980; Schlitzer et al., 2018) (Fig. 3). Surface dissolved Ni concentrations range from 2 to 6 nmol kg^{-1}, while surface dissolved Cu concentrations range from 0.4–2.0 nmol kg^{-1}, with the lowest concentrations of both metals found at the northernmost stations in the SAZ (stations 7 and 8). The ratios of 'deep' (maximum depth of 1000 m in this study) to surface concentrations always remain <2 for Ni and Cu, while ratios for other nutrient-type metals and macronutrients are generally >2 and can, in some cases, reach >10–100. Consequently, a greater concentration range is observed spatially in surface waters for dissolved Ni and Cu than within single depth profiles, highlighting the contrast between Ni- and Cu-depleted surface waters north of the SAF and enriched waters south of the SAF. This is similar to dissolved Cr concentration data from the same transect (Rickli et al., 2019). Dissolved Ni and Cu concentrations in the SAZ and south of the PF compare well with previous data in the Atlantic and Indian sectors of the Southern Ocean (Westerlund et al., 1986; Löscher, 1999; Ellwood, 2008; Cameron and Vance, 2014; Heller and Croot, 2015; Cloete et al., 2018; Wang et al., 2019). Dissolved Ni concentrations are slightly elevated in subsurface samples on the Kerguelen Plateau relative to samples off the plateau, as found in previous data from the region (Wang et al., 2019). This may reflect changes in circulation, enhanced regeneration from organic matter or a lithogenic source.

Dissolved Ni distributions are correlated with dissolved NO_3 and PO_4 as well as with $Si(OH)_4$, as described previously in other basins (e.g. Sclater et al., 1976). The correlation between Ni and organic-associated macronutrients (PO_4, NO_3) follow a more consistent single slope (2.13 ± 0.07 mmol mol^{-1} for Ni-PO_4, $r^2 = 0.83$; Table 2, Fig. 4 e and g), similar to that observed previously in the SAZ (1.81 mmol mol^{-1}; Ellwood, 2008). However, our SAZ samples alone do not show a strong linear Ni-PO_4 correlation (Table 2). Dissolved Ni-$Si(OH)_4$ demonstrates a bimodal distribution. Stations north of the Subantarctic Front (stations 7 and 8) have low $Si(OH)_4$ and Ni concentrations, and a somewhat scattered Ni-$Si(OH)_4$ relationship with a high slope (0.12 ± 0.03 mmol mol^{-1}, $r^2 = 0.47$). The remaining stations, except for the terrestrially-influenced stations 11 and 12, cluster along a low-slope trend (0.018 ± 0.001 mmol mol^{-1}, $r^2 = 0.77$) with a much higher Ni intercept (Table 2), and both the slope and intercept agree well with previous reports from the Southern Ocean (Löscher, 1999; Wang et al., 2019); see Section 5.1 for a discussion of continental influence at stations 11 and 12. Our Ni-macronutrient relationships are clearly different from trends reported for a meridional section in the Atlantic sector of the Southern Ocean, where Ni-macronutrient trends showed less robust relationships and lower slopes (Cloete et al., 2018).

A global compilation suggests that the two-part Ni-$Si(OH)_4$ distribution is better described as a non-linear, curved Ni-$Si(OH)_4$ trend at $0 < Si(OH)_4 < 50$ μmol kg^{-1} followed by a linear, low Ni-$Si(OH)_4$ slope at higher $Si(OH)_4$ concentrations, as we observe in the Southern Ocean. However, the exact trends differ between the Atlantic, Indian and Pacific Oceans. Global compilations for Ni-PO_4 do not yield as uniform a linear trend as we observe in the Southern Ocean (Fig. 4f and h). Our data, which highlight different Ni-macronutrient trends in different Southern Ocean regimes and a robust, singular Ni-PO_4 correlation not found in the global ocean, suggest that there is distinct Ni cycling in this region. This is supported by similarities in other Ni-macronutrient datasets in the Southern Ocean (Löscher, 1999; Wang et al., 2019; Archer et al., 2020), suggesting that the observed Ni-macronutrient features may be found throughout the Southern Ocean. A better understanding of these unique Southern Ocean Ni-macronutrient trends could improve our understanding of controls on the Ni biogeochemical cycle.

Stations from the SAZ show a linear Cu-PO_4 relationship, in agreement with previous data from the SAZ (Ellwood, 2008), though the relationship becomes non-linear when incorporating data from south of the PF (Table 2, Fig. 4i). Copper shows a better linear correlation with $Si(OH)_4$ over our whole data set (m = 0.016 ± 0.000 mmol mol^{-1}, $r^2 = 0.90$), though latitudinal differences in the exact slope remain. We find higher Cu-$Si(OH)_4$ slopes at stations 7 and 8 (0.028 ± 0.004 mmol mol^{-1}, $r^2 = 0.75$), and increasing slopes from the PFZ to south of the SACCB (from 0.010 ± 0.001 mmol mol^{-1} to 0.015 ± 0.001 mmol mol^{-1}, respectively), as described previously (Löscher, 1999; Boye et al., 2012) (Table 2). The slope for all our data is similar to that observed previously in the PFZ (Löscher, 1999) and in the global ocean as a whole (Table 2, Fig. 4 k and l).

4.5. Lead

Dissolved Pb distributions show either a surface minimum or relatively uniform concentrations within the upper 1000 m (Fig. 3). The highest dissolved Pb concentrations are observed at the northernmost station (station 8), in the SAZ, which likely reflects Pb enrichment in the Indian Ocean due to anthropogenic input (Echegoyen et al., 2014; Lee et al., 2015). Lead distributions at the lower latitude stations 8 and 9 are similar to those observed previously in this region (Ellwood, 2008); however, the absolute concentrations we find in our samples, collected in January 2017, are about 3–5 pmol kg^{-1} lower than in samples collected in the same region in July 2006. This is a difference of ~20–33% (cf. this study and Ellwood, 2008), which may reflect sampling season and/or the phasing-out of leaded fuels in New Zealand by 1996 (Wilson and Horrocks, 2008) and in Australia from the 1970s to early 2000s (Kristensen, 2015), as well as more generally in Africa, India, and Southeast Asia in the late 1990s through the 2000s (Thomas and Kwong, 2001; Lee et al., 2014).

Lead concentrations decrease southward both in surface and subsurface waters, and enrichments the subsurface waters in the SAZ and PFZ are observed relative to similar water masses at higher latitudes (Fig. 3, Supplemental Fig. 4). Concentrations of Pb are below 10 pmol kg^{-1} south of the PF in the Pacific sector of the Southern Ocean, in agreement with observations in the Indian sector (Echegoyen et al., 2014). These concentrations are among the lowest found in the upper 1000 m in the global ocean (Supplemental Fig. 5). This likely reflects the isolation of the Southern Ocean from natural and anthropogenic aerosol sources, limiting surface input (e.g. Duce et al., 1991), as well as a continued regional decrease in leaded fuel combustion (Thomas and Kwong, 2001; von Storch et al., 2003; Lee et al., 2014). A slight enrichment of Pb is observed from 50–200 m at stations 18 and 19, south of and in the Drake Passage, relative to the adjacent sampling sites, though the reason for this is unclear.

North of 50° S, we observe a Pb enrichment along the isopycnal associated with AAIW ($\gamma^n \approx 27.3$ kg m^{-3}) relative to surface waters, as described previously (Boye et al., 2012; Echegoyen et al., 2014; Lee et al., 2015). Lower dissolved Pb are found at higher latitude along this isopycnal (Supplemental Fig. 4), which previous studies in the Indian Ocean have attributed to lower atmospheric Pb deposition in water more recently at the surface (Echegoyen et al., 2014; Lee et al., 2015).

5. Discussion of regional features and nutriclines

5.1. The Mertz Glacier Polynya

Surface concentrations for macronutrients and most trace metals at the Mertz Glacier Polynya (Stations 11 & 12) are substantially lower than in surface waters of nearby stations south of the SACCB (e.g. Station 13), and correlations between trace metals and macronutrients show divergences at these stations (grey symbols in Fig. 4) compared to the rest of our data. Trace metal depletion is most pronounced for Zn and Cd, with surface concentrations in the Mertz Glacier Polynya as low as 0.19 nmol kg^{-1} and 0.050 nmol kg^{-1} respectively, an order of magnitude lower than at surface water in nearby stations. For Zn, concentrations approach values found to be co-limiting in the open ocean (Chappell et al., 2016). The high degree of Zn depletion may explain the extent of Cd depletions through cambialistic substitution for Zn or limited specificity in upregulated metal transport systems, as inferred in culture studies (Lee and Morel, 1995; Sunda and Huntsman, 2000) and suggested previously in the Southern Ocean (Abouchami et al., 2014).

Salinity data from the Mertz Glacier Polynya show an influence of meltwater input; however, the salinity difference is relatively small (~3%) compared to the observed trace metal and macronutrient depletions. Consequently, mixing of seawater with potential freshwater sources (snow, landfast ice, and pure freshwater) with their own respective trace metal concentrations to yield a 3% decrease in salinity cannot explain the observed trace metal depletions (up to 1 order of magnitude). Dilution of 3% from the different freshwater sources results in similar expected surface metal concentrations when considering single endmember mixing (seawater-snow, seawater-ice, seawater-pure freshwater). The calculations are described further in the supplemental material and Supplemental Tables 2 and 3. High CTD fluorescence at these sites (Supplemental Fig. 6) suggests that the strong metal and macronutrient deficits observed are most likely due to biological uptake, or, in the case of Pb, due to scavenging by biogenic particles. Polynyas elsewhere near the Antarctic continent are known to have substantial Fe sources (e.g. Sherrell et al., 2015), and therefore input of Fe at the Mertz Glacier Polynya may be relieving Fe-limitation and fueling biological productivity. While such an Fe enrichment is not easily identifiable in our data, as surface Fe concentrations at these stations are uniformly low, this may be explained by biological uptake and Fe removal (together with other trace metals) at the edges of the system, as observed in the Amundsen Sea (Sherrell et al., 2015).

Biological uptake ratios of metals to phosphate ($Me:PO_4$) can be calculated from the observed surface depletion of metals and macronutrients relative to expected surface concentrations from freshwater dilution, and are shown in Table 3 along with comparisons to literature data. We calculate an average $Me:PO_4$ uptake ratio for $Zn:PO_4$ of 3.1 ± 0.4 mmol mol^{-1}, $Cu:PO_4$ of 0.69 ± 0.10 mmol mol^{-1}, $Ni:PO_4$ of 1.3 ± 0.2 mmol mol^{-1}, and $Cd:PO_4$ of 0.53 ± 0.07 mmol mol^{-1}. These uptake ratios compare well with Me:P ratios in natural phytoplankton assemblages from the Southern Ocean (Twining and Baines, 2013) and are similar to inferred $Cu:PO_4$ and $Zn:PO_4$ uptake reported by Sherrell et al. (2015) (Table 3). Furthermore, our calculated ratios match observed Cd:P (Cullen et al., 2003; Lane et al., 2009) and Ni:P (Twining et al., 2004) in Fe-limited phytoplankton, and correspond with Zn:P observed in incubation experiments with partial, but incomplete, relief of Fe-limitation (+0.2 nmol L^{-1} Fe, partial limitation reflected in growth rate, Cullen et al., 2003). The agreement between the metal uptake we calculate for the Mertz Glacier Polynya and natural Fe-limited phytoplankton (Cullen et al., 2003; Twining et al., 2004; Lane et al., 2009; Twining and Baines, 2013) suggests that phytoplankton in the Mertz Glacier Polynya still experience some degree of Fe-limitation.

Our inferred $Ni:PO_4$ uptake (1.3 ± 0.2 mmol mol^{-1}) is much higher than that inferred by Sherrell et al. (2015) (0.29 mmol mol^{-1}); however, it is similar to the $Ni-PO_4$ slope we find in all our samples when omitting stations 7 and 8 (1.56 ± 0.08 nmol μmol^{-1}). While surface waters in the Mertz Glacier polynya have dissolved Zn and PO_4 concentrations in the range where a low-slope $Zn-PO_4$ trend is observed in the global ocean, it is the high-slope section (5.08 ± 0.34 mmol mol^{-1}) which better corresponds to the $Zn:PO_4$ uptake ratio we infer (3.1 ± 0.4 mmol mol^{-1}) (Fig. 4, Table 2). This may reflect coupling between Zn and PO_4 uptake, export and regeneration in these samples at high $Zn:PO_4$ ratios, as previously described in the Southern Ocean (Twining et al., 2014; Vance et al., 2017; de Souza et al., 2018; Roshan et al., 2018). The $Cd:PO_4$ uptake we infer agrees well with the $Cd-PO_4$ trend observed in our data. The $NO_3:PO_4$ we calculate (14.5 mol mol^{-1}) is between the Redfield ratio of 16 and the N:P previously observed in high-latitude phytoplankton (N:P = 13, Martiny et al., 2013), and in agreement with trends previously reported in the Atlantic sector (Nolting and de Baar, 1994; Weber and Deutsch, 2010).

The strong general agreement in observed metal depletions and inferred metal:macronutrient uptake ratios between the Amundsen Sea Polynya (Sherrell et al., 2015) and the Mertz Glacier Polynya (this study) highlights the importance of polynya systems in highly localized removal and subsequent biological export of trace metals and macronutrients to depth. This stands in stark contrast to surrounding waters with persistently elevated Ni, Cu, Zn, Cd and macronutrient concentrations in surface waters (e.g. Croot et al., 2011; Baars et al., 2014; Garcia et al., 2014; Sherrell et al., 2015; Cloete et al., 2018; this study). These coastal polynya systems, which have been characterized in terms of extent and seasonality of biological productivity (Arrigo and van Dijken, 2003) but for which trace metal data are limited, are a promising region to better understand biological export of metals and metal-macronutrient coupling in the Southern Ocean.

5.2. The impact of the Kerguelen and Balleny Islands on the distributions Fe, macronutrients and other trace metals

The supply of Fe from Antarctic and Subantarctic island margins to surface Fe-limited phytoplankton communities in the Southern Ocean has been well documented (e.g. Blain et al., 2001; Bakker et al., 2007; Gerringa et al., 2012; Hatta et al., 2013; Holmes et al., 2019). Consistent with these studies, we find elevated Fe concentrations downstream of the Kerguelen Islands (stations 3 and 4). Without a pre-Kerguelen endmember for comparison, it is difficult to precisely constrain the impact of the islands. However, we do find elevated subsurface concentrations of Ni, Cu, NO_3 and PO_4, as well as elevated $Si(OH)_4$ in the deepest samples, at stations 3 and 4 downstream of the Kerguelen Plateau relative to the more distal station 5 (Fig. 3).

The strong role that frontal systems play in regulating metal and macronutrient distributions near the Kerguelen Islands has been highlighted previously (Wang et al., 2019). Therefore, other island systems away from strong frontal gradients, such as the Balleny Islands, may prove useful for better constraining the local impact of Subantarctic and Antarctic islands on biogeochemical cycling. Surface Fe concentrations at station 14, downstream of the Balleny Islands, are higher than those immediately upstream of the islands (station 15) as well as further downstream and upstream (stations 13 and 16, respectively) (Fig. 3, Supplemental Fig. 7). Station 13 also shows elevated Fe near 100 m ($\gamma^n \approx 27.9$ kg m^{-3}), within the winter mixed later. Near-surface waters of station 15, upstream of the islands, are also enriched in Fe (100–300 m, $28.0 < \gamma^n < 28.1$ kg m^{-3}), indicating subsurface Fe in the region may have another source in addition to the islands. Nevertheless, the prominent elevated surface and near-surface concentrations seen at stations 14 and 13, respectively, indicate that the islands are a local Fe source for surface phytoplankton communities, and that this may be enhanced following deep mixing events.

The Balleny Islands, whether due to changes in mixing and circulation, potential benthic and land input, or changes in biological uptake following Fe addition, also appear to influence the distributions of macronutrients and other trace metals. Concentrations of PO_4, NO_3, Zn

Table 3
Inferred biological uptake at the Mertz Glacier Polynya. Uptake magnitudes and metal:PO_4 uptake ratios are inferred for biological uptake by the difference between observed and expected concentrations in surface waters of the Mertz Glacier Polynya. Inferred Me:PO_4 uptake ratios are compared to Me:P measured in Southern Ocean phytoplankton (Bulk phytoplankton composition before ([1]) and after ([2]) Fe addition incubations, Cullen et al., 2003; Synchrotron X-Ray Fluorescence data from single phytoplankton cells from south of the PF ([3]), Twining and Baines, 2013) and Me:PO_4 uptake ratios inferred from dissolved distributions in the Amundsen Sea ([4]) (Sherrell et al., 2015). Calculations are described in more detail in the supplemental material and Supplemental Tables 2 and 3.

	Zn	Cu	Ni	Cd	Pb	PO_4	Si	NO_3
	nmol kg^{-1}	nmol kg^{-1}	nmol kg^{-1}	nmol kg^{-1}	pmol kg^{-1}	μmol kg^{-1}	μmol kg^{-1}	μmol kg^{-1}
Inferred biological uptake (non-dilution metal deficit)	3.00	0.65	1.24	0.51	3.13	1.07	16.8	15.1
Inferred biological uptake (non-dilution metal deficit)	2.88	1.65	1.29	0.49	5.29	0.85	18.8	12.6

	Zn:P	Cu:P	Ni:P	Cd:P	N:P
	nmol μmol^{-1}	nmol μmol^{-1}	nmol μmol^{-1}	nmol μmol^{-1}	mol mol^{-1}
Me:PO_4 Uptake, Station 11	2.82	0.62	1.17	0.48	14.2
Me:PO_4 Uptake, Station 12	3.40	0.76	1.51	0.58	14.8
Average Me:PO_4, Stns 11 & 12	3.11 ± 0.41	0.69 ± 0.10	1.34 ± 0.24	0.53 ± 0.07	14.5 ± 0.05
Southern Ocean Lit. Me:P or Me:PO_4	11.09 ± 0.67[1], 2.02–4.05[2], ~3–20[3], 3.37[4]	1.44 ± 0.11[1], 0.43–0.63[2], 0.69[4]	~0.3–1.6[3], 0.29[4]	1.29 ± 0.07[1], 0.34–0.63[2]	NA

and Cd are elevated in surface samples downstream of the islands, while surface Si concentrations are depleted downstream of the islands (stations 14 and 13), relative to waters upstream (station 15). Cadmium and Zn isotope studies have suggested that elevated surface concentrations are the result of lower utilisation of Cd and Zn by phytoplankton due to the natural Fe fertilization (Sieber et al., 2019b; Sieber et al., 2020). Below the surface, elevated Si and Zn concentrations are found at station 15 below $\gamma^n = 28.0$ kg m^{-3} (~100 m depth) compared to similar isopycnals downstream of the islands. In deeper waters at station 14, immediately downstream of the islands, low concentrations of Si and, to a lesser extent, Cu are found relative to other stations. The reason for these differences is unclear at present, and may reflect complex changes in hydrography near the islands as well as the impact of Fe input on biological uptake, as well as potential metal scavenging in deeper waters (e.g. John and Conway, 2014; Roshan et al., 2018; Weber et al., 2018).

5.3. The nutriclines of macro- and micronutrients

Nutriclines, defined as the maximum of the derivative of the nutrient concentration depth profile ($\partial/\partial z$), are shown for PO_4, NO_3, Si, Fe, Zn and Cd in Fig. 5, along with the oxycline ($\partial O_2/\partial z$ minimum), pycnocline ($\partial\gamma^n/\partial z$ maximum) and γ^n in the upper 500 m. Nutriclines provide information on how species are removed from surface waters, regenerated at depth, redistributed by subsurface circulation, and how the mixing of subsurface water into the surface ocean would impact the supply of macro- and micronutrients. Low surface-to-deep dynamic ranges for Cu and Ni (surface:deep >0.5, see section 4.4) result in weak or ambiguous nutriclines (not shown). Low metal and macronutrient concentrations throughout the upper 1000 m in the SAZ (stations 7 and 8), along with the absence of a strong oxycline and more uniform potential density throughout the upper 500 m, result in minor to no nutriclines for most elements in this zone (Figs. 3 & 5).

The pycnocline is found within the upper 100 m. The oxycline is generally found between 50 and 300 m and is often associated with the transition from AAIW ($\gamma^n = 27.3$ kg m^{-3}) to UCDW ($\gamma^n = 27.8$ kg m^{-3}) where these water masses are present. Nutriclines for NO_3 (the nitricline) and PO_4 (the phosphocline), which generally co-occur, are mostly found within the upper 100 m (Fig. 5). These shallow depth horizons indicate that NO_3 and PO_4 can be made more readily available to surface communities with the seasonal deepening of the mixed layer (see also Dong et al., 2008). The nutricline for $Si(OH)_4$ is found slightly deeper than the phosphocline at approximately half of the stations (e.g. 5–6, 10, 15–17, 19–20), which can help to isolate $Si(OH)_4$ from surface waters relative to other macronutrients. This is in agreement with distributions of $Si(OH)_4$ in the surface ocean (Sarmiento et al., 2004; Garcia et al., 2014) and with comprehensive studies of preferential Si export from regions of the Southern Ocean (e.g. Brzezinski et al., 2003; Sarmiento et al., 2004). However, these differences are generally minor. The nutricline for Cd corresponds with the phosphocline, demonstrating a coupling of Cd and PO_4. Nutriclines for Zn show similarities to both PO_4 and $Si(OH)_4$, with some stations better correlating with PO_4 (e.g. station 16) and some more similar to $Si(OH)_4$ (stations 10, 17, 19–20). Though, differences between macronutrients are minor and the nutricline for Zn corresponds well to both macronutrients.

5.4. The ferricline and implications for (micro-)nutrient supply to the euphotic zone

As the Southern Ocean is Fe-limited, Fe supply to the surface ocean and the relative Fe supply compared to macronutrients is a topic of keen interest. Multiple methods of comparing the relative availability of Fe and macronutrients have been employed in the Southern Ocean, including Fe:PO_4 (e.g. Sohrin et al., 2002), Fe:NO_3 (e.g. Croot et al., 2007; Ellwood et al., 2008; Bowie et al., 2009), Fe* calculated relative to PO_4 (e.g. Parekh et al., 2005; Boyd et al., 2007; Bowie et al., 2009; Lannuzel et al., 2011b) and relative to $Si(OH)_4$ (Bowie et al., 2009), and the depth of the ferricline (e.g. Tagliabue et al., 2014). These studies of relative Fe supply in the Southern Ocean indicate that subsurface waters, should they reach the surface ocean, supply insufficient Fe relative to macronutrients compared to phytoplankton growth requirements. Here we add to this potential subsurface Fe supply discussion with our new Southern Ocean dataset.

The nutricline for Fe (the ferricline) generally falls between 100 and 300 m depth (Fig. 5), in agreement with ferricline isopycnal horizons ($\gamma^n \geq 27.5$ kg m^{-3}) previously reported in the Southern Ocean (Tagliabue et al., 2014). The ferricline depths we observe can still extend below the maximal winter mixed layer (Dong et al., 2008), therefore isolating subsurface Fe-enriched waters from the surface ocean. At stations with potential continental or near-surface marine sediment sources, for example near the Kerguelen Plateau (stations 3–4) and near the Balleny Islands (stations 14–15), the ferricline depth is more shallow, as described previously near Kerguelen (Blain et al., 2008; Schallenberg et al., 2018), and is comparable to that of macronutrients. This likely reflects subsurface sources of Fe, highlighting the well-documented importance of Subantarctic and Antarctic islands in supplying Fe (Blain et al., 2001; Blain et al., 2008; Schallenberg et al., 2018), as well as altering deepwater flow to bring (micro-)nutrient-rich

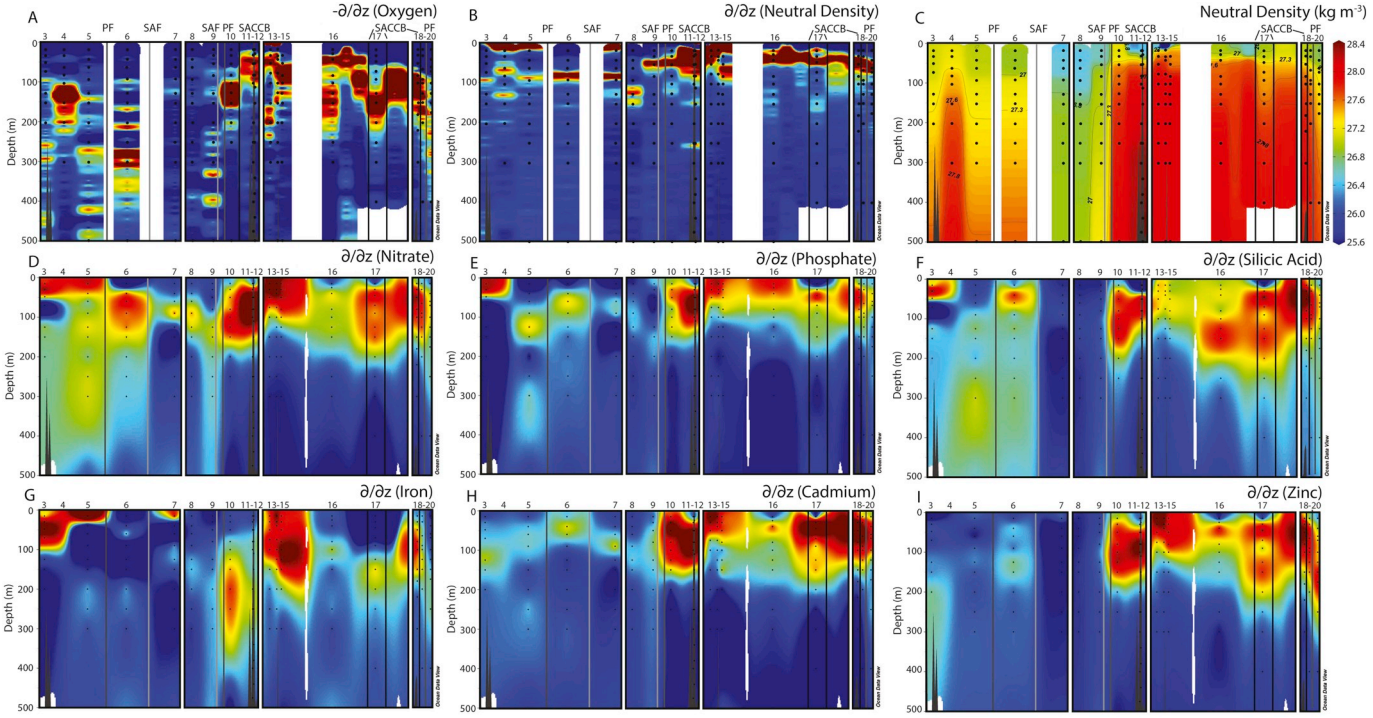

Fig. 5. Nutriclines for macronutrients and biologically cycled metals. First derivative plots ($\partial/\partial z$) for metals and macronutrients are shown to identify nutriclines ($\partial/\partial z$ maxima), along with the oxycline ($\partial O_2/\partial z$ minimum, a) and pycnocline ($\partial \gamma^n/\partial z$ maximum, b) and γ^n (c). Nutriclines are shown for NO_3 (the nitricline, d), PO_4 (the phosphocline, e) and $Si(OH)_4$ (f) and for Fe (the ferricline, g) Cd (h) and Zn (i). Warmer colors indicate high $\partial/\partial z$, with the nutricline identified as the warmest colors for each metal or macronutrient. Because oxygen consumption is associated with organic matter respiration and increases in macro- and micronutrients, the color scale for the oxycline has been inverted such that warm and cool colors match the nutricline plots. Positions of fronts (SAF, PF and SACCB; labelled) are shown as solid lines with colors matching the fronts in Fig. 1. Plots are broken by white bars to differentiate primarily zonal sections (stations 3–7, 12–18) and primarily meridional sections (stations 8–12, 18–20).

deepwater closer to the surface (Sokolov & Rintoul, 2007; Grand et al., 2015). However, the ferricline is found below the nitricline and phosphocline at most other stations, including at the Mertz Glacier Polynya. With a ferricline found deeper than the nitricline and phosphocline, Fe is more efficiently isolated from the surface ocean than macronutrients and deepwater entrainment accesses macronutrient-enriched waters before Fe-enriched waters, in support of previous studies in the Southern Ocean (e.g. Tagliabue et al., 2014).

The limited supply of Fe relative to macronutrients is further illustrated by Fe:NO_3 ratios throughout our transect, which remain $\leq$0.01 mmol mol^{-1}, values characteristic of Fe-limited regions (Martin et al., 1989; Ellwood et al., 2008), except at sites proximal to localized Fe sources (subsurface waters near the Kerguelen Plateau, Balleny Islands and Antarctic Peninsula) and at the macronutrient-depleted stations 7 and 8 (Fig. 6). Furthermore, Fe:NO_3 ratios fall well below minimum Fe:N in natural marine phytoplankton cells (0.06 mmol mol^{-1}, calculated from reported Fe:P assuming Redfield N:P of 16; Twining and Baines, 2013) and are within ranges for Fe-limited phytoplankton cultures growing at half of their Fe-replete growth rates (0.003–0.015 mmol mol^{-1}, calculated from Fe:C assuming Redfield C:P of 106; Strzepek et al., 2011). Apart from localized sources (e.g. lithogenic, dust, sea ice), deep mixing is the main Fe source to the surface in the Southern Ocean (Tagliabue et al., 2014). Our observed Fe:NO_3 values indicate that deep mixing, regardless of the absolute depths to which it reaches, will generally supply an excess of macronutrients over Fe relative to requirements for non Fe-limited phytoplankton growth, as reported previously (Parekh et al., 2005; Croot et al., 2007; Ellwood et al., 2008; Bowie et al., 2009; Lannuzel et al., 2011a).

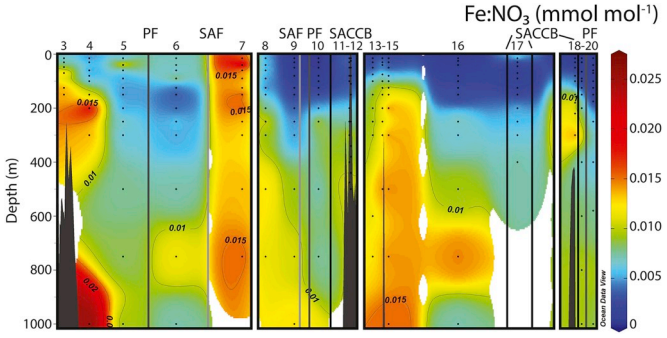

Fig. 6. ACE dissolved iron to nitrate ratios. A section plot of Fe:NO_3 to 1000 m is shown for the same section as in Figs. 2, 3 & 5. Labelled contours identify Fe:NO_3 = 0.01, 0.015 and 0.02 nmol µmol^{-1}. Positions of fronts (SAF, PF and SACCB; labelled) are shown as solid lines with colors corresponding to those used in Figs. 1. Plots are broken by white bars to differentiate primarily zonal sections (stations 3–7, 12–18) and primarily meridional sections (stations 8–12, 18–20).

6. Conclusions

The distribution of trace metals in the regions of the Southern Ocean studied here highlight the importance of biologically-driven cycles; however, latitudinal differences were as large or larger than surface-to-deep gradients, highlighting the interplay between biological drawdown and circulation in the Southern Ocean. We find that Pb concentrations decrease from the SAZ to south of the SACCB, and that Pb concentrations across all our data are among the lowest found in the global ocean. This likely reflects the isolation of the Southern Ocean from anthropogenic sources. Along the γ^n = 27.3 kg m^{-3} isopycnal

surface, associated with AAIW, Pb concentrations are lower in waters more recently in contact with the atmosphere, possibly reflecting decreases in atmospheric sources over time as leaded fuel use continues to decrease both locally and globally.

Zinc distributions correlate well with those of $Si(OH)_4$, with strong surface depletion of both elements north of the SACCB during our sampling in austral summer. The Zn-$Si(OH)_4$ slope within our data corresponds well with the global Zn-$Si(OH)_4$ relationship, which reflects the role that exported Southern Ocean waters play in forming the global Zn-$Si(OH)_4$ relationship (Vance et al., 2017; de Souza et al., 2018; Roshan et al., 2018; Weber et al., 2018; Sieber et al., 2020). South of the PF, Zn is correlated with PO_4, with a similar slope to that found at elevated Zn and PO_4 concentrations in the Atlantic Ocean (Wyatt et al., 2014). Overall, our Cd-PO_4 data are well correlated and show high slopes, similar to previous findings for the Southern Ocean (e.g. Baars et al., 2014). However, there are latitudinal differences in Cd-PO_4 slopes, with slopes increasing from the SAZ to the AZ. This may reflect the importance of Fe limitation and metal-metal antagonisms for Cd:PO_4 uptake in the Southern Ocean, and highlights the impact that exported Southern Ocean waters can have on the global Cd-PO_4 correlation, as indicated in previous studies (e.g. Frew and Hunter, 1992; Quay et al., 2015; Middag et al., 2018). Latitudinal variability is also observed for the Cu-$Si(OH)_4$ relationship, as previously described in the Southern Ocean (Löscher, 1999; Boye et al., 2012). We observe Ni-macronutrient correlations for both PO_4 and $Si(OH)_4$ that differ from the global relationships but are consistent with previous Southern Ocean studies (Löscher, 1999; Wang et al., 2019). This may indicate distinct Ni-macronutrient cycling in the Southern Ocean, and should be explored further to build a mechanistic understanding of the process(es) responsible for this.

We find that high productivity in the Mertz Glacier polynya drives substantial metal and macronutrient removal from surface waters. Our inferred metal:macronutrient uptake ratios correspond well with cellular quotas in Southern Ocean phytoplankton (Ni:P, Cu:P, Zn:P, Cd:P) and suggest that phytoplankton in the Mertz Glacier Polynya experience some degree of Fe limitation. Our study adds to the literature addressing the importance of coastal Antarctic polynya systems in driving high localized biological productivity in an Fe-limited region, and the impact that this productivity has on trace metal and macronutrient cycling and export. Such regions are a promising environment for future process studies on metal and macronutrient cycling, especially considering the impact of changing climate on the Southern Ocean and coastal ice dynamics (Tamura et al., 2008; Rignot et al., 2008).

The Kerguelen Plateau is a local source of dissolved Fe, as previously identified (e.g. Blain et al., 2001), and we identify the Balleny Islands as a previously-uncharacterized local source of Fe to surface waters. At the Balleny Islands, the distributions of NO_3, PO_4 and Si $(OH)_4$, Zn and Cd in surface waters and of $Si(OH)_4$, Cu and Zn in subsurface waters differ between stations upstream and downstream of the islands. This may be due to Fe addition modifying biological uptake of metals and macronutrients (Sieber et al., 2019b; Sieber et al., 2020), as well as changes in circulation and potential scavenging in subsurface waters. More detailed studies at these and other Antarctic islands away from the influence of frontal systems can help to better constrain the Fe input of such islands, and the influences of Fe input and circulation changes on the distributions of macronutrients and other trace metals.

The ferricline was found deeper than the nitricline at most stations, demonstrating the isolation of Fe, relative to macronutrients, from surface phytoplankton communities. Additionally, Fe:NO_3 ratios were indicative of Fe limiting conditions (Fe:NO_3 < 0.01 mmol mol^{-1}) in all samples except at locations near terrestrial or sediment sources (the Kerguelen Plateau, Balleny Islands and the Antarctic Peninsula), or in waters with very low macronutrient concentrations (stations 7 and 8). Therefore, considering that deep mixing is the main source of Fe to much of the Southern Ocean (Tagliabue et al., 2014), nutricline depths and nutrient ratios in subsurface waters indicate that mixing would ultimately act to maintain Fe limitation in the absence of other Fe sources.

Research data

Data are available in the supplementary material as well as in the Zenodo repository (metal data doi: https://doi.org/10.5281/zenodo.3634411; macronutrient data (Hassler and Ellwood, 2019) doi: https://doi.org/10.5281/zenodo.2616606; ctd data (Henry et al., 2019) doi: https://doi.org/10.5281/zenodo.3247384).

Acknowledgements

This work was supported by the Swiss National Science Foundation (grant PP00P2_172915). ACE was a scientific expedition carried out under the auspices of the Swiss Polar Institute (SPI), supported by funding from the ACE Foundation and Ferring Pharmaceuticals. We are grateful to the Chief Scientist, the late David Walton, and the captain and crew of the R/V Akademik Tryoshnikov for their continuous support during the voyage. We acknowledge Scarlett Trimborn for use of the AWI clean sampling container and, along with Tina Brenneis, for nutrient analyses. We acknowledge sampling assistance from Damien Cabanes and Marion Fourquez. TMC acknowledges support from the University of South Florida. CH was supported by the Swiss National Science Foundation (PP00P2_138955 and PP00P2_166197). GFdS was supported by a Marie Skłodowska-Curie Research Fellowship under EU Horizon 2020 (SOSiC; 708407).

Appendix A. Supplementary data

Supplementary data to this article can be found online at https://doi.org/10.1016/j.marchem.2020.103773.

References

Abouchami, W., Galer, S.J.G., de Baar, H.J.W., Middag, R., Vance, D., Zhao, Y., Klunder, M., Mezger, K., Feldmann, H., Andreae, M.O., 2014. Biogeochemical cycling of cadmium isotopes in the Southern Ocean along the Zero Meridian. Geochim. Cosmochim. Acta 127, 348–367. https://doi.org/10.1016/j.gca.2013.10.022.

Anderson, R.F., Mawji, E., Cutter, G.A., Measures, C.I., Jeandel, C., 2014. GEOTRACES: changing the way we explore ocean chemistry. Oceanogr. 27 (1), 50–61.

Archer, C., Andersen, M.B., Cloquet, C., Conway, T.M., Dong, S., Ellwood, M., Moore, R., Nelson, J., Rehkämper, M., Rouxel, O., et al., 2017. Inter-calibration of a proposed new primary reference standard AA-ETH Zn for zinc isotopic analysis. J. Anal. At. Spectrom. 32, 415–419. https://doi.org/10.1039/C6JA00282J.

Archer, C., Vance, D., Milne, A., Lohan, M.C., 2020. The oceanic biogeochemistry of nickel and its isotopes: new data from the South Atlantic and the Southern Ocean biogeochemical divide. Earth Planet. Sci. Lett. 535, 116118. https://doi.org/10.1016/j.epsl.2020.116118.

Ardelan, M.V., Holm-Hansen, O., Hewes, C.D., Reiss, C.S., Silva, N.S., Dulaiova, H., Steinnes, E., Sakshaug, E., 2010. Natural iron enrichment around the Antarctic Peninsula in the Southern Ocean. Biogeoscience 7, 11–25. https://doi.org/10.5194/bg-7-11-2010.

Ardyna, M., Lacour, L., Sergi, S., d'Ovidio, F., Sallée, J.B., Rembauville, M., Blain, S., Tagliabue, A., Schlitzer, R., Jeandel, Arrigo, K.R., Claustre, H., 2019. Hydrothermal vents trigger massive phytoplankton blooms in the Southern Ocean. Nat. Commun. 10, 2451. https://doi.org/10.1038/s41467-019-09973-6.

Arrigo, K.R., van Dijken, G.L., 2003. Phytoplankton dynamics within 37 Antarctic coastal polynya systems. J. Geophys. Res. 108 (C8). https://doi.org/10.1029/2002JC001739.

de Baar, H.J.W., Saager, P.M., Nolting, R.F., Meer, J., 1994. Cadmium versus phosphate in the world ocean. Mar. Chem. 46 (3), 261–281. https://doi.org/10.1016/0304-4203(94)90082-5.

de Baar, H.J.W., de Jong, J.T.M., Nolting, R.F., Timmermans, K.R., van Leeuwe, M.A., Bathmann, U., Rutgers van der Loeff, M.R., Sildam, J., 1999. Low dissolved Fe and the absence of diatom blooms in remote Pacific waters of the Southern Ocean. Mar. Chem. 66 (1–2), 1–34. https://doi.org/10.1016/S0304-4203(99)00022-5.

Baars, O., Abouchami, W., Galer, S.J.G., Boye, M., Croot, P.L., 2014. Dissolved cadmium in the Southern Ocean: distribution, speciation, and relation to phosphate. Limnol. Oceanogr. 59 (2), 385–399. https://doi.org/10.4319/lo.2014.59.2.0385.

Bakker, D.C.E., Nielsdóttir, M.C., Morris, P.J., Venables, H.J., Watson, A.J., 2007. The island mass effect and biological carbon uptake for the subantarctic Crozet Archipelago. Deep-Sea Res. II **54** (18-20), 2174–2190. https://doi.org/10.1016/j.dsr2.2007.06.009.

Barrett, P.M., Resing, J.A., Grand, M.M., Measures, C.I., Landing, W.M., 2018. Trace element composition of suspended particulate matter along three meridional CLIVAR sections in the Indian and Southern Oceans: Impact of scavenging on Al distributions. Chem. Geol. 502, 15–28. https://doi.org/10.1016/j.chemgeo.2018.06.015.

Blain, S., Tréguer, P., Belviso, S., Bucciarelli, E., Denis, M., Desabre, S., Fiala, M., Jézéquel, V.M., Le Fèvre, J., et al., 2001. A biogeochemical study of the island mass effect in the context of the iron hypothesis: Kerguelen Islands, Southern Ocean. Deep Sea Res. I. 48 (1), 163–187. https://doi.org/10.1016/S0967-0637(00)00047-9.

Blain, S., Quéguiner, B., Armand, L., Belviso, S., Bombled, B., Bopp, L., Bowie, A., Brunet, C., Brussaard, C., Carlotti, et al., 2007. Effect of natural iron fertilization on carbon sequestration in the Southern Ocean. Nature. 446, 1070–1074. https://doi.org/10.1038/nature05700.

Blain, S., Sarthou, G., Laan, P., 2008. Distribution of dissolved iron during the natural iron-fertilization experiment KEOPS (Kerguelen Plateau, Southern Ocean). Deep-Sea Res. II 55 (5–7), 594–605. https://doi.org/10.1016/j.dsr2.2007.12.028.

Borges Mendes, C.R., Kerr, R., Tavano, V.M., Cavalheiro, F.A., Eiras Garcia, C.A., Gauns Dessai, D.R., Anilkumar, N., 2015. Cross-front phytoplankton pigments and chemi-taxonomic groups in the Indian sector of the Southern Ocean. Deep-Sea Res. II 118 (B), 221–232. https://doi.org/10.1016/j.dsr2.2015.01.003.

Bowie, A.R., Lannuzel, D., Remenyi, T.A., Wagener, T., Lam, P.J., Boyd, P.W., Guieu, C., Townsend, A.T., Trull, T.W., 2009. Biogeochemical iron budgets of the Southern Ocean south of Australia: Decoupling of iron and nutrient cycles in the subantarctic zone by the summertime supply. Glob. Biogeochem. Cy. 23 (4). https://doi.org/10.1029/2009GB003500. (14 pp).

Boyd, P.W., Jickells, T., Law, C.S., Blain, S., Boyle, E.A., Buesseler, K.O., Coale, K.H., Cullen, J.J., de Baar, H.J.W., et al., 2007. Mesoscale iron enrichment experiments 1993-2005: synthesis and future directions. Science. 315 (5812), 612–617. https://doi.org/10.1126/science.1131669.

Boye, M., Wake, B., Lopez Garcia, P., Brown, J., Baker, A.R., Achterberg, E.P., 2012. Distributions of dissolved trace metals (Cd, Cu, Mn, Pb, Ag) in the southeastern Atlantic and the Southern Ocean. Biogeoscience 9, 3231–3246. https://doi.org/10.5194/bg-9-3231-2012.

Boyle, E.A., Sclater, F., Edmund, J.M., 1976. On the marine geochemistry of cadmium. Nature. 263, 42–44. https://doi.org/10.1038/263042a0.

Boyle, E.A., John, S., Abouchami, W., Adkins, J.F., Echegoyen-Sanz, Y., Ellwood, M., Flegal, A.R., Fornace, K., Gallon, C., Galer, S., et al., 2012. GEOTRACES IC1 (BATS) contamination-prone trace element isotopes Cd, Fe, Pb, Zn, Cu, and Mo intercalibration. Limnol. Oceanogr. Methods 10 (9), 653–665. https://doi.org/10.4319/lom.2012.10.653.

Bruland, K.W., 1980. Oceanographic distributions of cadmium, zinc, nickel, and copper in the North Pacific. Earth Planet. Sci. Lett. 47 (2), 176–198. https://doi.org/10.1016/0012-821X(80)90035-7.

Bruland, K.W., Knauer, G.A., Martin, J.H., 1978. Zinc in north-east Pacific water. Nature. 271, 741–743. https://doi.org/10.1038/271741a0.

Brzezinski, M.A., Dickson, M.-L., Nelson, D.M., Sambrotto, R., 2003. Ratios of Si, C and N uptake by microplankton in the Southern Ocean. Deep-Sea Res. II 50, 619–633. https://doi.org/10.1016/S0967-0645(02)00587-8.

Bucciarelli, E., Blain, S., Tréguer, P., 2001. Iron and manganese in the wake of the Kerguelen Islands (Southern Ocean). Mar. Chem. 73 (1), 21–36. https://doi.org/10.1016/S0304-4203(00)00070-0.

Cameron, V., Vance, D., 2014. Heavy nickel isotope compositions in rivers and the oceans. Geochim. Cosmochim. Acta 128, 195–211. https://doi.org/10.1016/j.gca.2013.12.007.

Chappell, P.D., Vedmati, J., Selph, K.E., Cyr, H.A., Jenkins, B.D., Landry, M.R., Moffett, J.W., 2016. Preferential depletion of zinc within Costa Rica upwelling dome creates conditions for zinc co-limitation of primary production. J. Plankton Res. 38 (2), 244–255. https://doi.org/10.1093/plankt/fbw018.

Cloete, R., Loock, J.C., Mtshali, T., Fietz, S., Roychoudhury, A.N., 2018. Winter and summer distributions of Copper, Zinc and Nickel along the International GEOTRACES Section GIPY05: Insights into deep winter mixing. Chem. Geol. 511, 342–357. https://doi.org/10.1016/j.chemgeo.2018.10.023.

Coale, K.H., Johnson, K.S., Chavez, F.P., Buesseler, K.O., Barber, K.T., Brzezinski, M.A., Cochlan, W.P., Millero, F.J., Falkowski, P.G., et al., 2004. Southern Ocean iron enrichment experiment: carbon cycling in high- and low-Si waters. Science. 304 (5669), 408–414. https://doi.org/10.1126/science.1089778.

Conway, T.M., Rosenberg, A.D., Adkins, J.F., John, S.G., 2013. A new method for precise determination of iron, zinc and cadmium stable isotope ratios in seawater by double-spike mass spectrometry. Anal. Chim. Act. 793, 44–52. https://doi.org/10.1016/j.aca.2013.07.025.

Croot, P.L., Frew, R.D., Sander, S., Hunter, K.A., Ellwood, M.J., Pickmere, S.E., Abraham, E.R., Law, C.S., Smoth, M.J., Boyd, P.W., 2007. Physical mixing effects on iron biogeochemical cycling: FeCycle experiment. J. Geophys. Res. 115, C06015. https://doi.org/10.1029/2006JC003748.

Croot, P.L., Baars, O., Streu, P., 2011. The distribution of dissolved zinc in the Atlantic sector of the Southern Ocean. Deep-Sea Res. II 58 (25–26), 2707–2719. https://doi.org/10.1016/j.dsr2.2010.10.041.

Cullen, J.T., 2006. On the nonlinear relationship between dissolved cadmium and phosphate in the modern global ocean: could chronic iron limitation of phytoplankton growth cause the kink? Limnol. Oceanogr. 51 (3), 1369–1380. https://doi.org/10.4319/lo.2006.51.3.1369.

Cullen, J.T., Chase, Z., Coale, H.H., Fitzwater, S.E., Sherrell, R.M., 2003. Effect of iron limitation on the cadmium to phosphorus ratio of natural phytoplankton assemblages from the Southern Ocean. Limnol. Oceanogr. 48 (3), 1079–1087. https://doi.org/10.4319/lo.2003.48.3.1079.

Dong, S., Sprintall, J., Gille, S.T., Talley, L., 2008. Southern Ocean mixed-layer depth from Argo float profiles. J. Geophys. Res. Oc. 113, C6. https://doi.org/10.1029/2006JC004051.

Duce, R.A., Liss, P.S., Merrill, J.T., Atlas, E.L., Buar-Menard, P., Hicks, B.B., Miller, J.M., Prospero, J.M., Arimoto, R., Church, T.M., et al., 1991. The atmospheric input of trace species to the world ocean. Glob. Biogeochem. Cy. 5 (3), 192–259. https://doi.org/10.1029/91GB01778.

Echegoyen, Y., Boyle, E.A., Lee, J.M., Gamo, T., Obata, H., Norisuye, K., 2014. Recent distribution of lead in the Indian Ocean reflects the impact of regional emissions. Proc. Natl. Acad. Sci. U. S. A. 111 (43), 15328–15331. https://doi.org/10.1073/pnas.1417370111.

Ellwood, M.J., 2008. Wintertime trace metal (Zn, Cu, Ni, Cd, Pb and Co) and nutrient distributions in the Subantarctic Zone between 40–52°S; 155–160°E. Mar. Chem. 112 (1–2), 107–117. https://doi.org/10.1016/j.marchem.2008.07.008.

Ellwood, M.J., Boyd, P.W., Sutton, P., 2008. Winter-time dissolved iron and nutrient distributions in the Subantarctic Zone from 40–52S; 155–160E. Geophys. Res. Lett. **35** (11). https://doi.org/10.1029/2008GL033699. 6 pp.

Ellwood, M.J., Bowie, A.R., Baker, A., Gault-Ringold, M., Hassler, C., Law, C.S., Maher, W.A., Marriner, A., Nodder, S., et al., 2018. Insights into the biogeochemical cycling of iron, nitrate, and phosphate across a 5300 km South Pacific Zonal Section (153°E–150°W). Glob. Biogeochem. Cy. 32, 187–207. https://doi.org/10.1002/2017GB005736.

Ellwood, M.J., Strzepek, R., Chen, X., Trull, T.W., Boyd, P.W., 2020. Some observations on the biogeochemical cycling of zinc in the Australian sector of the Southern Ocean: a dedication to Keith Hunter. Mar. Freshw. Res. https://doi.org/10.1071/MF19200. 19 pp.

Franck, V.M., Brzezinski, M.A., Coale, K.H., Nelson, D.M., 2000. Iron and silicic acid concentrations regulate Si uptake north and south of the Polar Frontal Zone in the Pacific Sector of the Southern Ocean. Deep-Sea Res. II 47 (15–16), 3315–3338. https://doi.org/10.1016/S0967-0645(00)00070-9.

Frew, R.D., 1995. Antarctic bottom water formation and the global cadmium to phosphorus relationship. Geophys. Res. Lett. 22 (17), 2349–2352. https://doi.org/10.1029/95GL02238.

Frew, R.D., Hunter, K.A., 1992. Influence of Southern Ocean waters on the cadmium–-phosphate properties of the global ocean. Nature. 360, 144–146. https://doi.org/10.1038/360144a0.

Fripiat, F., Cavagna, A.J., Savoye, N., Dehairs, F., André, L., Cardinal, D., 2011. Isotopic constraints on the Si-biogeochemical cycle of the Antarctic Zone in the Kerguelen area (KEOPS). Mar. Chem. 123 (1–4), 11–22. https://doi.org/10.1016/j.marchem.2010.08.005.

Garcia, H.E., Locarnini, R.A., Boyer, T.P., Antonov, J.I., Baranova, O.K., Zweng, M.M., Reagan, J.R., Johnson, D.R. (2014) World Ocean Atlas 2013, Volume 4: Dissolved Inorganic Nutrients (phosphate, nitrate, silicate). S. Levitus, Ed., A. Mishonov Technical Ed.; NOAA Atlas NESDIS 76, 25 pp.

Gerringa, L.J.A., Alderkamp, A.C., Laan, P., Thuróczy, C.E., de Baar, H.J.W., Mills, M.M., van Dijken, G.L., van Haren, H., Arrigo, K.R., 2012. Iron from melting glaciers fuels the phytoplankton blooms in the Amundsen Sea (Southern Ocean): Iron biogeochemistry. Deep-Sea Res. II 71-71, 16–31. https://doi.org/10.1016/j.dsr2.2012.03.007.

Gibberd, M.J., Kean, E., Barlow, R., Thomalla, S., Lucas, M., 2013. Phytoplankton chemotaxonomy in the Atlantic sector of the Southern Ocean during late summer 2009. Deep Sea Res. I. 78, 70–78. https://doi.org/10.1016/j.dsr.2013.04.007.

Grand, M.M., Measures, C.I., Hatta, M., Hiscock, W.T., Landing, W.M., Morton, P.L., Buck, C.S., Barrett, P.M., Resing, J.A., 2015. Dissolved Fe and Al in the upper 1000 m of the eastern Indian Ocean: a high-resolution transect along 95°E from the Antarctic margin to the Bay of Bengal. Glob. Biogeochem. Cy. 29 (3), 375–396. https://doi.org/10.1002/2014GB004898.

Hanawa, K., Talley, L.D., 2001. Mode waters. In: Siedler, G., Church, J.A., Gould, J. (Eds.), Ocean Circulation and Climate – Observing and Modelling the Global Ocean. Academic Press, San Diego, pp. 373–386.

Hassler, C., Ellwood, M., 2019. Nutrient Concentration in Seawater Samples, Collected from the Underway Supply, CTD and Trace Metal Rosettes in the Southern Ocean During the Austral Summer of 2016/2017, On Board the Antarctic Circumnavigation Expedition (ACE). (Version 1.0) [Data Set]. https://doi.org/10.5281/zenodo.2616606.

Hatta, M., Measures, C.I., Selph, K.E., Zhou, M., Hiscock, W.T., 2013. Iron fluxes from the shelf regions near the South Shetland Islands in the Drake Passage during the austral-winter 2006. Deep-Sea Res. II 90, 89–101. https://doi.org/10.1016/j.dsr2.2012.11.003.

Heller, M.I., Croot, P.L., 2015. Copper speciation and distribution in the Atlantic sector of the Southern Ocean. Mar. Chem. 173, 253–268. https://doi.org/10.1016/j.marchem.2014.09.017.

Henry, T., Robinson, C., Haumann, F.A., Thomas, J., Hutchings, J., Houssais, M., Schuback, N., Tsukernik, M., Leonard, K., Masseì, G., 2019. Physical and Biogeochemical Oceanography from Conductivity, Temperature, Depth (CTD) Rosette Deployments During the Antarctic Circumnavigation Expedition (ACE). (Version 1.0) [Data set]. Zenodohttps://doi.org/10.5281/zenodo.3247384.

Hoffmann, L.J., Peeken, L., Lochte, K., 2008. Iron, silicate, and light co-limitation of three Southern Ocean diatom species. Polar Biol. 31, 1067–1080. https://doi.org/10.1007/s00300-008-0448-6.

Holmes, T.M., Wuttig, K., Chase, Z., van der Merwe, P., Townsend, A.T., Schallenberg, C., Tonnard, M., Bowie, A.R., 2019. Iron availability influences nutrient drawdown in the Heard and McDonald Islands region, Southern Ocean. Mar. Chem. 211, 1–14. https://doi.org/10.1016/j.marchem.2019.03.002.

Hutchins, D.A., Bruland, K.W., 1998. Iron-limited diatom growth and Si:N uptake ratios in a coastal upwelling regime. Nature. 393, 561–564. https://doi.org/10.1038/31203.

Jaccard, S.L., Hayes, C.T., Martinez Garcia, A., Hodell, D.A., Anderson, R.F., Sigman, D.M., Haug, G.H., 2013. Two Modes of Change in Southern Ocean Productivity Over

the Past Million Years. Science 339 (6126), 1419–1423. https://doi.org/10.1126/science.1227545.
John, S.G., Conway, T.M., 2014. A role for scavenging in the marine biogeochemical cycling of zinc and zinc isotopes. Earth Planet. Sci. Lett. 394, 159–167. https://doi.org/10.1016/j.epsl.2014.02.053.
Jones, E.M., Hoppema, M., Strass, V., Hauck, J., Salt, L., Ossebaar, S., Klaas, C., van Heuven, S.M.A.C., Wolf-Gladrow, D., Stöven, T., de Baar, H.J.W., 2017. Mesoscale features create hotspots of carbon uptake in the Antarctic Circumpolar Current. Deep-Sea Res. II 138, 39–51. https://doi.org/10.1016/j.dsr2.2015.10.006.
de Jong, J., Schoemann, V., Lannuzel, D., Croot, P., de Baar, H., Tison, J.L., 2012. Natural iron fertilization of the Atlantic sector of the Southern Ocean by continental shelf sources of the Antarctic Peninsula. J. Geophys. Res. 117https://doi.org/10.5194/bg-7-11-2010. (25 pp).
Klunder, M.B., Laan, P., Middag, R., de Baar, H.J.W., van Ooijen, J.C., 2011. Dissolved iron in the Southern Ocean (Atlantic sector). Deep-Sea Res. II 58 (25–26), 2678–2694. https://doi.org/10.1016/j.dsr2.2010.10.042.
Kopczynska, E.E., Dehairs, F., Elskens, M., Wright, S., 2001. Phytoplankton and micro-zooplankton variability between the Subtropical and Polar Fronts south of Australia: thriving under regenerative and new production in late summer. J. Geophys. Res. Oc. 106 (C12), 31597–31609. https://doi.org/10.1029/2000JC000278.
Kristensen, L.J., 2015. Quantification of atmospheric lead emissions from 70 years of leaded petrol consumption in Australia. Atmos. Environ. 111, 195–201. https://doi.org/10.1016/j.atmosenv.2015.04.012.
Lancelot, C., de Montety, A., Goosse, H., Becquevort, S., Schoemann, V., Pasquer, B., Vancoppenolle, M., 2009. Spatial distribution of the iron supply to phytoplankton in the Southern Ocean: a model study. Biogeoscience 6, 2861–2878. https://doi.org/10.5194/bg-6-2861-2009.
Lane, E.S., Semeniuk, D.M., Strzepek, R.F., Cullen, J.T., Maldonado, M.T., 2009. Effects of iron limitation on intracellular cadmium of cultured phytoplankton: Implications for surface dissolved cadmium to phosphate ratios. Mar. Chem. 115 (3-4), 155–162. https://doi.org/10.1016/j.marchem.2009.07.008.
Lannuzel, D., Bowie, A.R., Remenyi, T., Lam, P., Townsend, A., Ibisanmi, E., Butler, E., Wagener, T., Schoemann, V., 2011b. Distributions of dissolved and particulate iron in the sub-Antarctic and Polar Frontal Southern Ocean (Australian sector). Deep-Sea Res. II 58 (21 – 22), 2094–2112. https://doi.org/10.1016/j.dsr2.2011.05.027.
Lannuzel, D., Bowie, A.R., van der Merwe, P.C., Townsend, A.Y., Shoemann, V., 2011a. Distribution of dissolved and particulate metals in Antarctic sea ice. Mar. Chem. 124, 134–146. https://doi.org/10.1016/j.marchem.2011.01.004.
Lee, J.G., Morel, F.M.M., 1995. Replacement of zinc by cadmium in marine phytoplankton. Mar. Ecol. Prog. Ser. 127, 305–309. https://doi.org/10.3354/meps127305.
Lee, J.M., Boyle, E.A., Echegoyen-Sanz, Y., Fitzsimmons, J.N., Zhang, R., Kayser, R.A., 2011. Analysis of trace metals (Cu, Cd, Pb, and Fe) in seawater using single batch nitrilotriacetate resin extraction and isotope dilution inductively coupled plasma mass spectrometry. Anal. Chim. Acta 686, 93–101. https://doi.org/10.1016/j.aca.2010.11.052.
Lee, J.M., Boyle, E.A., Nurhati, I.S., Meltzner, A.J., Suwargdi, B., 2014. Coral-based history of lead and lead isotopes of the surface Indian Ocean since the mid-20th century. Earth Planet. Sci. Lett. 398, 37–47. https://doi.org/10.1016/j.epsl.2014.04.030.
Lee, J.M., Boyle, E.A., Gamo, T., Obata, H., Norisuye, K., Echegoyen, Y., 2015. Impact of anthropogenic Pb and ocean circulation on the recent distribution of Pb isotopes in the Indian Ocean. Geochim. Cosmochim. Acta 170, 126–144. https://doi.org/10.1016/j.gca.2015.08.013.
Löscher, B.M., 1999. Relationships among Ni, Cu, Zn, and major nutrients in the Southern Ocean. Mar. Chem. 67 (1–2), 67–102. https://doi.org/10.1016/S0304-4203(99)00050-X.
Lumpkin, R., Speer, K., 2007. Global ocean meridional overturning. J. Phys. Oc. 37, 2550–2562. https://doi.org/10.1175/JPO3130.1.
Mahowald, N.M., Hamilton, D.S., Mackey, K.R.M., Moore, J.K., Baker, A.R., Scanza, R.A., Zhang, Y., 2018. Aerosol trace metal leaching and impacts on marine microorganisms. Nat. Commun. 9, 2614. https://doi.org/10.1038/s41467-018-04970-7.
Martin, J.H., 1990. Glacial-interglacial CO_2 chance: the iron hypothesis. Paleocean. Paleoclim. 5 (1), 1–13. https://doi.org/10.1029/PA005i001p00001.
Martin, J.H., Gordon, R.M., Fitzwater, S., Broenkow, W.W., 1989. Vertex: phytoplankton/iron studies in the Gulf of Alaska. Deep Sea Res. A. 36 (5), 649–680. https://doi.org/10.1016/0198-0149(89)90144-1.
Martin, J.H., Fitzwater, S.E., Gordon, R.M., 1990a. Iron deficiency limits phytoplankton growth in Antarctic waters. Glob. Biogeochem. Cy. 4 (1), 5–12. https://doi.org/10.1029/GB004i001p00005.
Martin, J.H., Gordon, M., Fitzwater, S.E., 1990b. Iron in Antarctic Waters. Nature 345, 156–158. https://doi.org/10.1038/345156a0.
Martínez-García, A., Rosell-Mel, A., Jaccard, S.L., Geibert, W., Sigman, D.M., Haug, G.H., 2011. Southern Ocean dust-climate coupling over the past four million years. Nature. 476, 312–316. https://doi.org/10.1038/nature10310.
Martiny, A.C., Pham, C.T.A., Primeau, F.W., Vrugt, J.A., Moore, K., Levin, S.A., Lomas, M.W., 2013. Strong latitudinal patterns in the elemental ratios of marine plankton and organic matter. Nat. Geosci. 6, 279–283. https://doi.org/10.1038/ngeo1757.
Measures, C.I., Vink, S., 2001. Dissolved Fe in the upper waters of the Pacific sector of the Southern Ocean. Deep-Sea Res. II 48 (19–20), 3919–3941. https://doi.org/10.1016/S0967-0645(01)00074-1.
Measures, C.I., Brown, M.T., Selph, K.E., Apprill, A., Zhou, M., Hatta, M., Hiscock, W.T., 2013. The influence of shelf processes in delivering dissolved iron to the HNLC waters of the Drake Passage. Antarctica. *Deep Sea Res. II*. 90, 77–88. https://doi.org/10.1016/j.dsr2.2012.11.004.
Middag, R., van Heuven, S.M.A.C., Bruland, K.W., de Baar, H.J.W., 2018. The relationship between cadmium and phosphate in the Atlantic Ocean unravelled. Earth Planet. Sci. Lett. 492, 79–88. https://doi.org/10.1016/j.epsl.2018.03.046.
Middag, R., de Baar, H.J.W., Bruland, K.W., 2019. The relationships between dissolved zinc and major nutrients phosphate and silicate along the GEOTRACES GA02 transect in the West Atlantic Ocean. Glob. Biogeochem. Cy. 33 (1), 63–84. https://doi.org/10.1029/2018GB006034.
Moore, J.K., Doney, S.C., Glover, D.M., Fung, I.Y., 2001. Iron cycling and nutrient-limitation patterns in surface waters of the World Ocean. Deep-Sea Res. II 49 (1–3), 463–507. https://doi.org/10.1016/S0967-0645(01)00109-6.
Moore, C.M., Mills, M.M., Arrigo, K.R., Berman-Frank, I., Bopp, L., Boyd, P.W., Galbraith, E.D., Geider, R.J., Guieu, C., Jaccard, S.L., et al., 2013. Processes and patterns of oceanic nutrient limitation. Nat. Geosci. 6, 701–710. https://doi.org/10.1038/ngeo1765.
Nolting, R.F., de Baar, H.J.W., 1994. Behaviour of nickel, copper, zinc and cadmium in the upper 300 m of a transect in the Southern Ocean (57°–62°S, 49°W). Mar. Chem. 45 (3), 225–242. https://doi.org/10.1016/0304-4203(94)90006-X.
Nolting, R.F., de Baar, H.J.W., Van Bennekom, A.J., Masson, A., 1991. Cadmium, copper and iron in the Scotia Sea, Weddell Sea and Weddell/Scotia Confluence (Antarctica). Mar. Chem. 35 (1–4), 219–243. https://doi.org/10.1016/S0304-4203(09)90019-6.
Orsi, A.H., Whitworth III, T., Nowlin Jr., W.D., 1995. On the meridional extent and fronts of the Antarctic Circumpolar Current. Deep Sea Res. I. 42 (5), 641–673. https://doi.org/10.1016/0967-0637(95)00021-W.
Parekh, P., Follows, M.J., Boyle, E.A., 2005. Decoupling of iron and phosphate in the global ocean. Glob. Biogeochem. Cy. 19 (2). https://doi.org/10.1029/2004GB002280. (16 pp).
Pollard, R.T., Salter, I., Sanders, R.J., Lucas, M., Moore, C.M., Mills, R.A., Statham, P.J., Allen, J.T., Baker, A.R., Bakker, D.C.E., et al., 2009. Southern Ocean deep-water carbon export enhanced by natural iron fertilization. Nature 457, 577–580. https://doi.org/10.1038/nature07716.
Quay, P., Cullen, J., Landing, W., Morton, P., 2015. Processes controlling the distributions of Cd and PO_4 in the ocean. Glob. Biogeochem. Cy. 29 (6), 830–841. https://doi.org/10.1002/2014GB004998.
Rickli, J., Janssen, D.J., Hassler, C., Ellwood, M.J., Jaccard, S.L., 2019. Chromium biogeochemistry and stable isotope distribution in the Southern Ocean. Geochim. Cosmochim. Acta. https://doi.org/10.1016/j.gca.2019.07.033.
Rignot, E., Bamber, J.L., van den Broeke, M.R., Davis, C., Li, Y., van de Berg, W.J., van Meijgaard, E., 2008. Recent Antarctic ice mass loss from radar interferometry and regional climate modelling. Nat. Geosci. 1, 106–110. https://doi.org/10.1038/ngeo102.
Roshan, S., DeVries, T., Wu, J., Chen, G., 2018. The internal cycling of zinc in the ocean. Glob. Biogeochem. Cy. **32** (12), 1833–1849. https://doi.org/10.1029/2018GB006045.
Sambrotto, R.N., Matsuda, A., Vaillancourt, R., Brown, M., Langdon, C., Jacobs, S.S., Measures, C., 2003. Summer plankton production and nutrient consumption patterns in the Mertz Glacier Region of East Antarctica. Deep-Sea Res. II 50 (8–9), 1393–1414. https://doi.org/10.1016/S0967-0645(03)00076-6.
Sarmiento, J.L., Gruber, N., Brzezinski, M.A., Dunne, J.P., 2004. High-latitude controls of thermocline nutrients and low latitude biological productivity. Nature. 427, 56–60. https://doi.org/10.1038/nature02127.
Sarmiento, J.L., Simeon, J., Gnanadesikan, A., Gruber, N., Key, R.M., Schlitzer, R., 2007. Deep ocean biogeochemistry of silicate and nitrate. Glob. Biogeochem. Cy. 21. https://doi.org/10.1029/2006GB002720.
Schallenberg, C., Bestley, S., Klocker, A., Trull, T.W., Davies, D.M., Gault-Ringold, M., Eriksen, R., Roden, N.P., Sander, S., et al., 2018. Sustained upwelling of subsurface iron supplies seasonally persistent phytoplankton blooms around the southern Kerguelen Plateau, Southern Ocean. J. Geophys. Res. Oc. 123 (8), 5986–6003. https://doi.org/10.1016/S0304-4203(00)00070-0.
Schlitzer, R., 2018. Ocean Data View. Available at. http://odv.awi.de.
Schlitzer, R., Anderson, R.F., Dodas, E.M., Lohan, M., Geibert, W., Tagliabue, A., Bowie, A., Jeandel, C., Maldonado, M., et al., 2018. The GEOTRACES Intermediate Data Product 2017. Chem. Geol. 493, 210–233. https://doi.org/10.1016/j.chemgeo.2018.05.040.
Sclater, F.R., Boyle, E., Edmond, J.M., 1976. On the marine geochemistry of nickel. Earth Planet. Sci. Lett. 31 (1), 119–128. https://doi.org/10.1016/0012-821X(76)90103-5.
Sedwick, P.N., Bowie, A.R., Trull, T.W., 2008. Dissolved iron in the Australian sector of the Southern Ocean (CLIVAR SR3 section): meridional and seasonal trends. Deep Sea Res. I. 55 (8), 911–925. https://doi.org/10.1016/j.dsr.2008.03.011.
Sherrell, R.M., Lagerström, M.E., Forsch, K.O., Stammerjohn, S.E., Yager, P.L., 2015. Dynamics of dissolved iron and other bioactive trace metals (Mn, Ni, Cu, Zn) in the Amundsen Sea Polynya, Antarctica. *Elem. Sci. Anth.* **3**, 000071. https://doi.org/10.12952/journal.elementa.000071.
Sieber, M., Conway, T.M., de Souza, D.F., Obata, H., Takano, S., Sohrin, Y., Vance, D., 2019a. Physical and biogeochemical controls on the distribution of dissolved cadmium and its isotopes in the Southwest Pacific Ocean. Chem. Geol. 511, 494–509. https://doi.org/10.1016/j.chemgeo.2018.07.021.
Sieber, M., Conway, T.M., de Souza, G.F., Hassler, C., Ellwood, M., Vance, D., 2019b. High-resolution Cd isotope systematics in multiple zones of the Southern Ocean from the Antarctic Circumnavigation Expedition. Earth Planet. Sci. Lett. 527, 115799. https://doi.org/10.1016/j.epsl.2019.115799.
Sieber, M., Conway, T.M., de Souza, G.F., Ellwood, M., Vance, D., 2020. Cycling of Zn and its isotopes across multiple zones of the Southern Ocean: insights from the Antarctic Circumnavigation Expedition. Geochim. Cosmochim. Acta 268, 310–324. https://doi.org/10.1016/j.gca.2019.09.039.
Sigman, D.M., Altabet, M.A., McCorkle, D.C., Francois, R., Fischer, G., 2000. The δ15N of nitrate in the Southern Ocean: Nitrogen cycling and circulation in the ocean interior. J. Geophys. Res. Oc. 105 (C8), 19599–19614. https://doi.org/10.1029/2000JC000265.
Sohrin, Y., Iwamoto, S., Matsui, M., Obata, H., Nakayama, E., Suzuki, K., Handa, N., Ishii,

M., 2002. The distribution of Fe in the Australian sector of the Southern Ocean. Deep Sea Res. I. 47, 55–84. https://doi.org/10.1016/S0967-0637(99)00049-7.
Sohrin, Y., Urushihara, S., Nakatsuka, S., Kono, T., Higo, E., Minami, T., Norisuye, K., Umetani, S., 2008. Multielemental determination of GEOTRACES key trace metals in seawater by ICPMS after preconcentration using an ethylenediaminetriacetic acid chelating resin. Anal. Chem. 80 (16), 6267–6273. https://doi.org/10.1021/ac800500f.
Sokolov, S., Rintoul, S.R., 2007. On the relationship between fronts of the Antarctic Circumpolar Current and surface chlorophyll concentrations in the Southern Ocean. J. Geohpys. Res. 112, C7. https://doi.org/10.1029/2006JC004072.
de Souza, G.F., Reynolds, B.C., Johnson, G.C., Bullister, J.L., Bourdon, B., 2012. Silicon stable isotope distribution traces Southern Ocean export of Si to the eastern South Pacific thermocline. Biogeoscience 9, 4199–4213. https://doi.org/10.5194/bg-9-4199-2012.
de Souza, G., Khatiwala, S.P., Hain, M.P., Little, S.H., Vance, D., 2018. On the origin of the marine zinc-silicon correlation. Earth Planet. Sci. Lett. 492, 22–34. https://doi.org/10.1016/j.epsl.2018.03.050.
von Storch, H., Costa-Cabral, M., Hagner, C., Feser, F., Pacyna, J., Pacyna, E., Kolb, S., 2003. Four decades of gasoline lead emissions and control policies in Europe: a retrospective assessment. Sci. Tot. Environ. 311 (1–3), 151–176. https://doi.org/10.1016/S0048-9697(03)00051-2.
Strzepek, R.F., Maldonado, M.T., Hunter, K.A., Frew, R.D., Boyd, P.W., 2011. Adaptive strategies by Southern Ocean phytoplankton to lessen iron limitation: uptake of organically complexed iron and reduced cellular iron requirements. Limnol. Oceanogr. 56 (6), 1983–2002. https://doi.org/10.4319/lo.2011.56.6.1983.
Sunda, W.G., Huntsman, S.A., 2000. Effect of Zn, Mn, and Fe on Cd accumulation in phytoplankton: Implications for oceanic Cd cycling. Limnol. Oceanogr. 45 (7), 1501–1516. https://doi.org/10.4319/lo.2000.45.7.1501.
Tagliabue, A., Sallée, J.B., Bowie, A.R., Lévy, M., Swart, S., Boyd, P.W., 2014. Surface-water iron supplies in the Southern Ocean sustained by deep winter mixing. Nat. Geosci. 7, 314–320. https://doi.org/10.1038/ngeo2101.
Talley, L.D., 2013. Closure of the global overturning circulation through the Indian, Pacific, and Southern Oceans: schematics and transports. Oceanography 26, 80–97.
Tamura, T., Ohshima, K.I., Nihashi, S., 2008. Mapping of sea ice production for Antarctic coastal polynyas. Geophys. Res. Lett. 35 (7). https://doi.org/10.1029/2007GL032903. (5 pp).
Thomas, V., Kwong, A., 2001. Ethanol as a lead replacement: phasing out leaded gasoline in Africa. En. Pol. 29 (13), 1133–1143. https://doi.org/10.1016/S0301-4215(01)00041-6.
Trull, T.W., Bray, S.G., Manganini, S.J., Honjo, S., Francois, R., 2001. Moored sediment trap measurements of carbon export in the Subantarctic and Polar Frontal zones of the Southern Ocean, south of Australia. J. Geophys. Res. Oc. 106 (C12), 31489–31509. https://doi.org/10.1029/2000JC000308.
Twining, B.S., Baines, S.B., 2013. The trace metal composition of marine phytoplankton. An. Rev. Mar. Sci. 5, 191–215. https://doi.org/10.1146/annurev-marine-121211-172322.
Twining, B.S., Baines, S.B., Fisher, N.S., 2004. Element stoichiometries of individual plankton cells collected during the Southern Ocean Iron Experiment (SOFeX). Limnol. Oceanogr. 49 (6), 2115–2128. https://doi.org/10.4319/lo.2004.49.6.2115.
Twining, B.S., Nodder, S.D., King, A.L., Hutchins, D.A., LeCleir, D.R., DeBruyn, J.M., Maas, E.W., Vogt, S., Wilhelm, S.W., Boyd, P.W., 2014. Differential remineralization of major and trace elements in sinking diatoms. Limnol. Oceanogr. 59 (3), 689–704. https://doi.org/10.4319/lo.2014.59.3.0689.
Vance, D., Little, S.H., de Souza, G.F., Khatiwala, S., Lohan, M.C., Middag, R., 2017. Silicon and zinc biogeochemical cycles coupled through the Southern Ocean. Nat. Geosci. 10, 202–206. https://doi.org/10.1038/ngeo2890.
Walton, D.W.H., Thomas, J., 2018. Cruise Report – Antarctic Circumnavigation Expedition (ACE) 20th December 2016-19th March 2017. https://doi.org/10.5281/zenodo.1443511.
Wang, R.M., Archer, C., Bowie, A.R., Vance, D., 2019. Zinc and nickel isotopes in seawater from the Indian Sector of the Southern Ocean: the impact of natural iron fertilization versus Southern Ocean hydrography and biogeochemistry. Chem. Geol. 511, 453–464. https://doi.org/10.1016/j.chemgeo.2018.09.010.
Weber, T.S., Deutsch, C., 2010. Ocean nutrient ratios governed by plankton biogeography. Nature. 467, 550–554. https://doi.org/10.1038/nature09403.
Weber, T., John, S., Tagliabue, A., DeVries, T., 2018. Biological uptake and reversible scavenging of zinc in the global ocean. Science. 361 (6397), 72–76. https://doi.org/10.1126/science.aap8532.
Westerlund, S.F.G., Anderson, L.G., Hall, P.O.J., Iverfeldt, Å., Van Der Loeff, M.R., S, B., 1986. Benthic fluxes of cadmium, copper, nickel, zinc and lead in the coastal environment. Geochim. Cosmochim. Acta 50 (6), 1289–1296. https://doi.org/10.1016/0016-7037(86)90412-6.
Wilson, N., Horrocks, J., 2008. Lessons from the removal of lead from gasoline for controlling other environmental pollutants: a case study from New Zealand. Environ. Health 7 (1). https://doi.org/10.1186/1476-069X-7-1.
Wyatt, N.J., Milne, A., Woodward, E.M.S., Rees, A.P., Browning, T.J., Bouman, H.A., Worsfold, P.J., Lohan, M.C., 2014. Biogeochemical cycling of dissolved zinc along the GEOTRACES South Atlantic transect GA10 at 40°S. Glob. Biogeochem. Cy. 28, 44–56. https://doi.org/10.1002/2013GB004637.
Xie, R.C., Galer, S.J.G., Abouchami, W., Rijkenberg, M.J.A., de Baar, H.J.W., De Jong, J., Andreae, M.O., 2017. Non-Rayleigh control of upper-ocean Cd isotope fractionation in the western South Atlantic. Earth Planet. Sci. Lett. 471, 94–103. https://doi.org/10.1016/j.epsl.2017.04.024.
Zhao, Y., Vance, D., Abouchami, W., de Baar, H.J.W., 2014. Biogeochemical cycling of zinc and its isotopes in the Southern Ocean. Geochim. Cosmochim. Acta 125, 653–672. https://doi.org/10.1016/j.gca.2013.07.045.